

Recent Advances in the Exploration of the Small-Scale Structure of the Quiet Solar Atmosphere: Vortex Flows, the Horizontal Magnetic Field, and the Stokes-V Line-Ratio Method

O. Steiner and R. Rezaei,

Kiepenheuer-Institut für Sonnenphysik, Schöneckstrasse 6, 79104 Freiburg, Germany

Abstract. We review (i) observations and numerical simulations of vortical flows in the solar atmosphere and (ii) measurements of the horizontal magnetic field in quiet Sun regions. First, we discuss various manifestations of vortical flows and emphasize the role of magnetic fields in mediating swirling motion created near the solar surface to the higher layers of the photosphere and to the chromosphere. We reexamine existing simulation runs of solar surface magnetoconvection with regard to vortical flows and compare to previously obtained results. Second, we review contradictory results and problems associated with measuring the angular distribution of the magnetic field in quiet Sun regions. Furthermore, we review the Stokes-V-amplitude ratio method for the lines Fe I $\lambda\lambda$ 630.15 and 630.25 nm. We come to the conclusion that the recently discovered two distinct populations in scatter plots of this ratio must not be interpreted in terms of “uncollapsed” and “collapsed” fields but stem from weak granular magnetic fields and weak canopy fields located at the boundaries between granules and the intergranular space. Based on new simulation runs, we reaffirm earlier findings of a predominance of the horizontal field components over the vertical one, particularly in the upper photosphere and at the base of the chromosphere.

1. Introduction

Two different topics are reviewed in this contribution. (1) Vortical flows, which have been observed to exist in the deep photosphere and in the chromosphere. Over the past three years, they have anew attracted the attention from observers and computational physicists. We attempt to find and emphasize interrelations between the various manifestations of vortical flows in the solar atmosphere. (2) The polarimetry of the horizontal magnetic field in quiet Sun regions. We review the disparate results that have been obtained in the past and highlight the difficulties associated with such measurements. We discuss biases and propose an alternative method for dealing with selection criteria. The main part of the second chapter is devoted to the Stokes-V amplitude-ratio method and the origin of the dichotomy observed in scatter plots of the V amplitude of Fe I 630.15 nm vs. the V amplitude of Fe I 630.25 nm.

2. Vortical Flows and Vortex Tubes

Vortical flows, swirls, whirlpools, vortex tubes in the solar atmosphere have become a focus of intense research in the past three years. This chapter presents a brief review of

this research focus and attempts a comparison of some of these results with simulations carried out with the CO5BOLD (Freytag et al. 2012) code by the authors.

Vortical flows in the photosphere of the Sun were reported long before the present revival. Most notably is the vortex flow of Brandt et al. (1988), which was a vortical movement of granules that persisted for 1.5 h. These authors conjectured that if such vortices were a common feature of the solar convection zone, they might “provide an important mechanism for heating of stellar chromospheres and coronae by twisting the footpoints of magnetic flux tubes”.

From numerical simulations, Nordlund (1985) reports “a circular motion around the center of the downdraft, and the circular velocity is amplified as the downdraft narrows (‘bath-tub’ or ‘inverted tornado’)”. The centripetal force associated with this vortical flow was so strong that the gas pressure gradient opposing it, apparently led to numerical difficulties because the gas pressure in the center of the downdraft became too small or negative. Similar to Brandt et al. (1988), he also wondered about the consequences of such ‘inverted tornadoes’ for the higher layers of the atmosphere and conjectured that “the fact that any vertical magnetic field lines in the surrounding photosphere must be carried towards, and ‘sucked into’, these downdrafts also makes the phenomenon potentially very important as source of hydromagnetic disturbances”.

Wang et al. (1995) computed from a time series of continuum images from the Pic du Midi Observatory the horizontal vector flow field and associated divergence and the vertical component of the curl and found that the curl is correlated with regions of negative divergence, suggesting excess vorticity in intergranular lanes. A similar result is reported by Pötzi & Brandt (2007).

2.1. Vortical Flows in the Photosphere

With the ever increasing spatial resolution and homogeneity of long duration image sequences thanks to larger apertures of ground based solar telescopes, to high order adaptive optics systems and advanced image restoration techniques, and thanks to space based and balloon borne telescopes, vortical flows on ever smaller scales became visible.

Table 1. Vortex properties as detected by Bonet et al. (2008, 2010). The numbers in parentheses in the second column refer to the number of vortices with clockwise (first) and counterclockwise (second) sense of rotation.

telescope	number of detected vortices [-]	space-time density [Mm ⁻² minute ⁻¹]	mean life-time [minutes]
SST	138 (68, 70)	1.8×10^{-3}	5.1
Sunrise	42 (15, 27)	3.1×10^{-3}	7.9

Thus, Bonet et al. (2008) discovered small whirlpools on the solar surface with a size similar to terrestrial hurricanes ($\lesssim 0.5$ Mm), using the Swedish Solar Telescope (SST). They detected them because some magnetic bright points follow a logarithmic spiral on their way to being engulfed by a downdraft. Their image sequences at disk-center show 0.9×10^{-2} vortices per square Mm, with a lifetime of the order of 5 minutes, and with no preferred sense of rotation (see Table 1). They repeated this kind of analysis

with data from the balloon borne solar telescope Sunrise (Barthol 2011) and obtained similar results (see Table 1) with the notable difference that from the Sunrise data, they detected a preferred sense of rotation of the vortices. They speculate that this might be due to the fact that the Sunrise image sequences were recorded away from the solar equator, different from the previously obtained SST data. Away from the equator, differential rotation may have introduced a preferred sense of rotation. It remains to be explored if this effect is indeed taking place.

Vargas Domínguez et al. (2011) study a region of $69'' \times 69''$ of quiet Sun that includes the field of view investigated by Bonet et al. (2008) and derive statistical properties of swirl motions in the photosphere. They confirm the value for the space-time density of Bonet et al. (2008) and find no significant preference in the sense of rotation.

On a slightly larger scale, Attie et al. (2009) identify two long lasting vortex flows located at supergranular junctions, based on two time series of granulation from the Hinode/SOT broad band imager. The first vortex flow lasts at least 1 h and is $\approx 20''$ wide, the second vortex flow lasts more than 2 h and is $\approx 27''$ wide. In one case, the corresponding magnetogram shows a magnetic element of polarity opposite to the magnetic field in the center of the vortex, moving around the vortex center. At the same time, there is enhanced Ca II emission at the vortex center, which suggests possible magnetic dissipation because of entwinement of the magnetic fields.

Balmaceda et al. (2010) report an observation of magnetic flux concentrations being dragged towards the center of a convective vortex motion in the solar photosphere from data, including magnetogram sequences, simultaneously acquired with the SST and the Solar Optical Telescope (SOT) of Hinode. They argue that these small-scale motions were “likely to play a role in heating the upper solar atmosphere by twisting magnetic flux tubes.” Likewise, Manso Sainz et al. (2011) find two instances of magnetic elements which describe a vortical motion on a scale of $\lesssim 400$ km, using spectro-polarimetric and magnetographic data obtained with Hinode.

2.2. Swirls in the Chromosphere

Using the Swedish Solar Telescope (SST) with the CRISP Fabry P  rot system, Wedemeyer-B  hm & Rouppe van der (2009) found in narrow-band filtergrams with a FWHF of 11.1 pm in the line core of Ca I 854.2 nm swirling motions in chromospheric layers of a quiet Sun region inside a coronal hole. There, the view is not obstructed by chromospheric filaments, which gives free sight to chromospheric layers that would not be easily accessible in more active regions (see Figure 1).

The size of the swirl events is comparable to large terrestrial typhoons but their physical origin is a very different one. This is obvious as co-temporal broad band images show close groups of photospheric bright points that move with respect to each other, right beneath the swirls. Since such bright points are a reliable signature of tiny magnetic flux concentrations in the photosphere, it is highly probable that the origin of the chromospheric swirls are to be found in these moving magnetic flux concentrations. The swirls also exhibit Doppler shifts of -2 to -4 km s $^{-1}$ with peak values of up to -7 km s $^{-1}$. There is no clear indication of a swirling motion of the bright points, but one can imagine that magnetic flux concentrations trapped in a photospheric swirl similar to the ones detected by Bonet et al. (2008, 2010) may start to rotate and lead to chromospheric disturbances that would be similar to the ones observed by Wedemeyer-B  hm & Rouppe van der Voort (2009) and similar as predicted by Nordlund (1985).

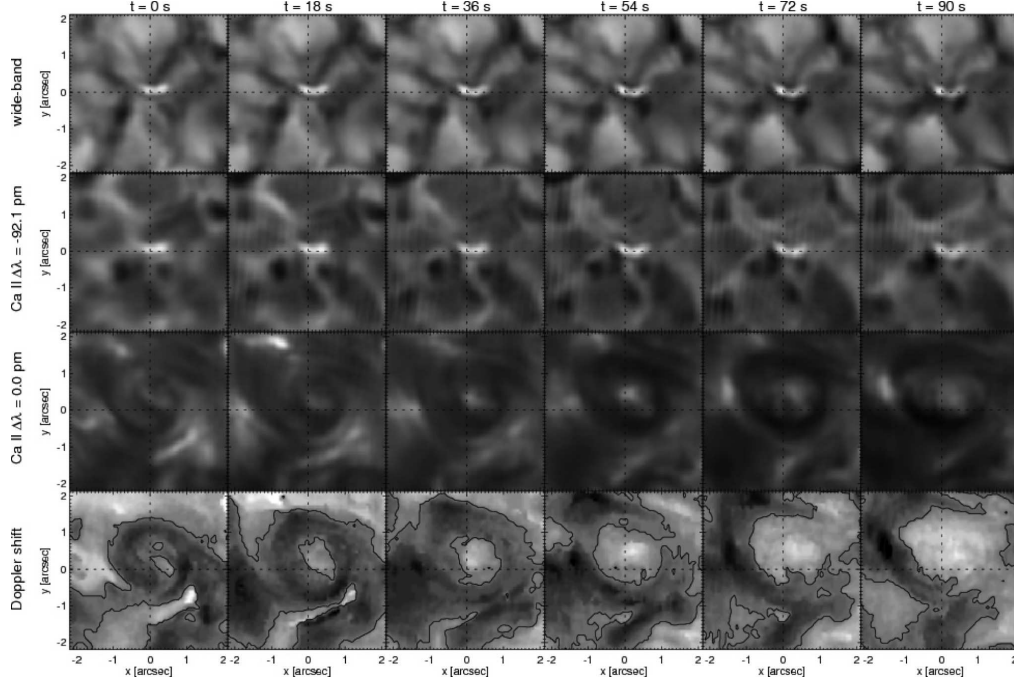


Figure 1. Temporal evolution of a swirl event as seen in close-ups of intensity maps in the wide-band (top row), Ca line wing (upper middle), Ca line core (lower middle), and Doppler shift (bottom). The black contours in the bottom row mark zero Doppler shift. The grey scale of the Doppler shift is from -5.5 to $+5.5 \text{ km s}^{-1}$ with negative values corresponding to blueshifts and thus upflows. Credit: Wedemeyer-Böhm & Rouppe van der Voort (2009) reproduced with permission © ESO.

On a considerably larger scale but also in quiet Sun regions, Zhang & Liu (2011) observe extreme-ultraviolet cyclones in all EUV channels of the Atmospheric Imaging Assembly (AIA) on board the Solar Dynamics Observatory (SDO). These cyclones seem to be rooted in rotating network magnetic fields that are simultaneously observed in the photosphere with the Helioseismic and Magnetic Imager (HMI; Schou et al. (2011)). They can last for several to more than 10 hr and are found to be associated with EUV brightenings (microflares) and EUV waves in their later phase. At this stage it is unclear if and what kind of connections between Wedemeyer-Böhm & Rouppe van der Voort's swirl and Zhang & Liu's cyclones may exist.

2.3. Numerical Simulations

Shelyag et al. (2011) carried out magnetic and non-magnetic three-dimensional numerical simulations of solar granulation with the MURaM code (Vögler 2011; Vögler et al. 2005) to analyze the generation of small-scale vortex motions in the solar photosphere. Starting with a magnetic field-free model, they observe the generation of swirls in the upper part of their model, as soon as a uniform, vertical magnetic field of 200 G strength is introduced. They find that the vortices in the upper photosphere are co-spatial with the magnetic field concentrations in the intergranular network in the lower photosphere that develop a short time after introduction of the magnetic field. Previously already,

Vögler (2004) found such a relation as well. It is of course tempting to identify these vortical flows, which obviously occur in connection with magnetic flux concentrations, with the chromospheric swirls of Wedemeyer-Böhm & Rouppe van der Voort (2009). But for this, maps of Ca I 854.2 nm would need to be synthesized from the simulation for a more direct comparison.

As an independent, qualitative confirmation of the results of Shelyag et al. (2011), we show in Figure 2 swirling motion that occurs in the upper part of a model atmosphere obtained from a simulation with the CO5BOLD code (Freytag et al. 2012; Beeck et al. 2012). We have carried out three equivalent simulation runs with a box size of $9.6 \times 9.6 \text{ Mm}^2$ and a depth of 2.8 Mm, where the average depth of $\tau_c = 1$ is at mid height. Figure 2 (top) shows a time instance of the velocity field as projected into the horizontal plane at a height of 1300 km above $\langle \tau_c \rangle = 1$ for the simulation run B0 without magnetic fields. Added in gray-scale is the temperature, which shows a meshwork of sharp temperature peaks, corresponding to shock fronts. The cellular flow field does not correspond to the granular flow field in the deep photosphere—rather it is an independent, rapidly evolving pattern at chromospheric heights (Wedemeyer et al. 2004). The longest arrows correspond to a velocity of about 14 km s^{-1} . No swirls are visible in this magnetic field-free simulation. Figure 2 (bottom) shows the corresponding flow at the same time instance from an equivalent simulation, v50, that started with a homogeneous vertical magnetic field of strength 50 G. The flow field is conspicuously different and the meshwork of shock waves is absent. Swirling, or undulatory motion is now omnipresent and must have been introduced through the magnetic field. A third equivalent simulation, h50, was carried out in which horizontal field of 50 G strength was advected by updrafts through the bottom boundary, similar to Steiner et al. (2008) or Stein & Nordlund (2006). This simulation shows again a flow pattern similar to the field-free case shown in Figure 2 (top) because in this case the magnetic field is more turbulent and complex and its average strength drops exponentially with height because of the many intricate loops that develop. These differences suggest that strong swirls in the upper atmosphere may best develop in case of a rather unipolar open field configuration as may occur at the base of a coronal hole.

In another independent study, Moll et al. (2012) carry out comparative simulations, similar to those shown in Fig. 2. They find a considerably different flow structure in the upper photospheric layers of two simulations: the non-magnetic simulation is dominated by a pattern of moving shock fronts while the magnetic simulation shows vertically extended vortices associated with magnetic flux concentrations. They note that both kinds of structures induce substantial local heating, in the magnetic case through Ohmic dissipation associated with the swirling motion.

Shelyag et al. (2011) also derive the equation for the vorticity $\omega = \nabla \times \mathbf{v}$ by taking the curl of the MHD momentum equation:

$$\begin{aligned} \frac{D\omega}{Dt} = & \overbrace{(\omega \cdot \nabla)\mathbf{v} - \omega(\nabla \cdot \mathbf{v})}^{\text{tilting and stretching } T_1} + \overbrace{\frac{1}{\rho^2} \nabla \rho \times \nabla p_{\text{gas}}}^{\text{baroclinic term } T_2} \\ & + \overbrace{\frac{1}{\rho^2} \nabla \rho \times \left[\nabla p_{\text{mag}} - \frac{1}{4\pi} (\mathbf{B} \cdot \nabla) \mathbf{B} \right]}^{\text{magnetic baroclinic term } T_3} + \overbrace{\frac{1}{4\pi \rho} \nabla \times (\mathbf{B} \cdot \nabla) \mathbf{B}}^{\text{magnetic tension } T_4}, \end{aligned} \quad (1)$$

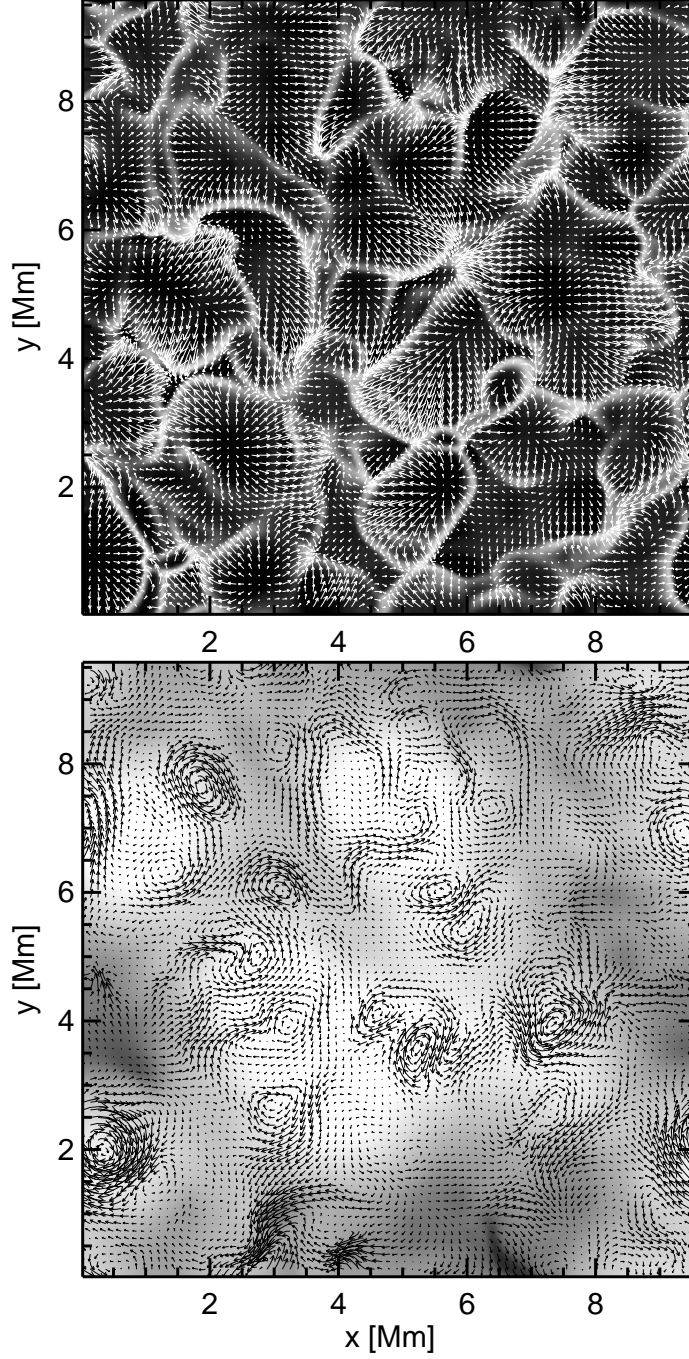


Figure 2. Time instances of the velocity field projected into the horizontal plane at 1300 km above $\langle \tau_c \rangle = 1$. Top: Magnetic field-free simulation B0. Overplotted in gray scale is the temperature. Temperature peaks delineate the meshwork of shock fronts. Bottom: Same time instance from the simulation, v50, which started with a homogeneous, vertical magnetic field of 50 G. Gray scales in the background show the logarithm of the field strength, $\log |B|$ from 1 to 100 G. The flow field is strikingly different from the field-free simulation and shock waves are absent. Longest arrows with a 1% area coverage have $v \geq 14 \text{ km s}^{-1}$ (top) and $v \geq 12 \text{ km s}^{-1}$ (bottom).

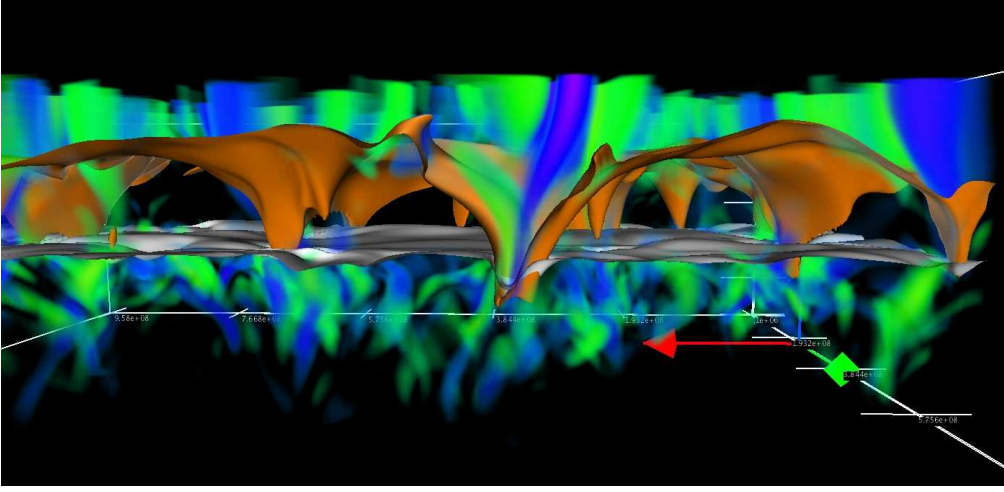


Figure 3. Vertical component of the vorticity, $\omega_z = (\nabla \times \mathbf{v})_z$ (green and blue for opposite signature) together with the surface (brown) of plasma $\beta = 1$. At the locations of magnetic flux concentrations, the $\beta = 1$ surface reaches through funnels into the deep photosphere and even below the surface (gray) of optical depth unity. In between the funnels, it forms a horizontally extending canopy at chromospheric levels. Above the $\tau_c = 1$ surface, vorticity is mainly confined to the region of $\beta \ll 1$. Below it, in the convection zone, vorticity is virtually everywhere present below intergranular lanes. The simulation was carried out with the CO5BOLD code (Freytag et al. 2012), the visualization with VAPOR 3D (Clyne et al. 2007). Courtesy, Ch. Nutto.

and study the individual sources for vorticity, T_1 to T_4 , in their simulation. Here, \mathbf{v} is the velocity, ρ the density, p_{gas} the gas pressure, and \mathbf{B} the magnetic field. They found that in the upper photosphere, the magnetic tension term is most important, while beneath the surface of optical depth unity, $\tau_c = 1$, the baroclinic term $|T_2|$ dominates $|T_4|$. Near $\tau_c = 1$, $|T_2|$ and $|T_4|$ are of similar magnitude. The other terms are of less importance.

Since the plasma β (ratio of thermal to magnetic pressure) generally decreases with height and assumes values smaller than one in the chromosphere and within magnetic flux concentrations in the photosphere, the results of Shelyag et al. (2011) indicate that vorticity may be generated in regions of small β through the magnetic tension term, i.e. by Lorentz forces. In fact, Figure 3 supports this conjecture. At the location of magnetic flux concentrations, the $\beta = 1$ surface (brown) reaches through funnels deep into the photosphere and even below the surface (gray) of optical depth unity. Above the surface of optical depth unity, vorticity (blue and green) is confined to within these funnels where $\beta \ll 1$. There is little vorticity outside the funnels in the photosphere, where $\beta \gg 1$. Clearly, this enhanced vorticity within the funnels must be generated by the magnetic field, possibly through the vortical motion flux concentrations are forced to follow when getting trapped within intergranular swirling sinkholes of the type found by Bonet et al. or Wang et al.

Kitiashvili et al. (2011) discover in their (field-free) simulations tiny circular ‘density holes’ in horizontal cross sections close to the solar surface. These ‘density holes’ with a density deficit of up to 60% are typically located at vertices of intergranular lanes but sometimes they also occur in the middle stretch of an intergranular lane. They are associated with a deficit in temperature of about 20%, a downdraft of up to 7 km s^{-1} ,

and swirling motion with often supersonic horizontal velocities. Kitiashvili et al.’s “whirlpools” must be the same object that Nordlund (1985) found to be a consequence of the centripetal force associated with a vortical flow. Underdense near-surface vertical vortices of similar properties are also found by Moll et al. (2011) from magnetoconvection simulations with the MURaM code (Vögler 2011; Vögler et al. 2005). According to these authors, they cause a local depression of the optical surface, which would potentially be observable as bright points in the dark intergranular lanes.

Most important, Kitiashvili et al. (2011) also found that whirlpools can attract and capture other swirls of opposite vorticity. They showed that this processes of vortex interaction, can cause the excitation of acoustic waves on the Sun. They conclude that strongly interacting vortices in the top layers of the convection zone, in particular the interaction of the vortices with opposite sign of vorticity, may play an important role in the excitation of solar acoustic oscillations. In their simulations, they did not find a preference in directions of the vortex rotation, which should be expected since neither the Coriolis force nor differential rotation is included. However, if the findings of a preferred sense of rotation of Bonet et al. (2010) should substantiate and if these swirls are indeed an important source of acoustic oscillations, one might speculate that this could have observable consequences for the p-mode oscillations. One could possibly expect reduced power at latitudes of enhanced differential rotation.

Figure 4 (top) shows the bolometric intensity of a simulation snapshot of the above mentioned field-free CO5BOLD simulation B0. Superimposed on the intensity map is the velocity field projected into the horizontal plane at the average optical depth unity. This is approximately, what could be derived from observations with the help of correlation tracking and equivalent techniques. The figure demonstrates, that swirling motions are not particularly conspicuous. In most vertices of inter-granular lanes, there is hardly any sign of swirling motion visible in this snapshot. Only at $(x, y) = (6000, 3000)$ km, there is clear evidence of a ‘whirlpool’. The situation changes drastically when examining the density at about 100 km below mean optical depth unity, which section is shown in Figure 4 (bottom). There, we can see small underdense circular areas with a diameter of ≈ 100 –200 km, which are associated with swirling motion, e.g., at $(x, y) = (3800, 3200)$ km, $(x, y) = (5000, 8500)$ km, $(x, y) = (1900, 8250)$ km, and twin swirls at $(x, y) = (5000, 7000)$ km. They have a density of typically 60% of the mean density, while the intergranular lanes have typically 115%. They also are typically 25–35% cooler than the average temperature. These findings qualitatively corroborate corresponding results by Kitiashvili et al. (2011) and Moll et al. (2011). We do not see a bright point in the bolometric intensity map at the location of the whirlpool as was reported by Moll et al. (2011) but this may be due to insufficient spatial resolution of the present simulation. There is no one-to-one correspondence of swirls visible at the solar surface and underdense vortices 120 km below it. For example, the conspicuous swirl visible at $(x, y) = (6000, 3000)$ km at the surface has no underdense counterpart 120 km beneath. On the other hand, the underdense swirl at $(x, y) = (3800, 3200)$ km seems to be associated with an intensity enhancement at the surface but not with a clear vortical flow. The twin swirls at $(x, y) = (5000, 7000)$ km are associated with a granular lane visible in the intensity map (Fig. 4 top). In fact, it looks like the two ‘footpoints’ of the horseshoe-like granular lane were leading into the twin sinkholes, forming all together a loop-like vortex tube. Granular lanes and vortex tubes are reviewed in the following subsection.

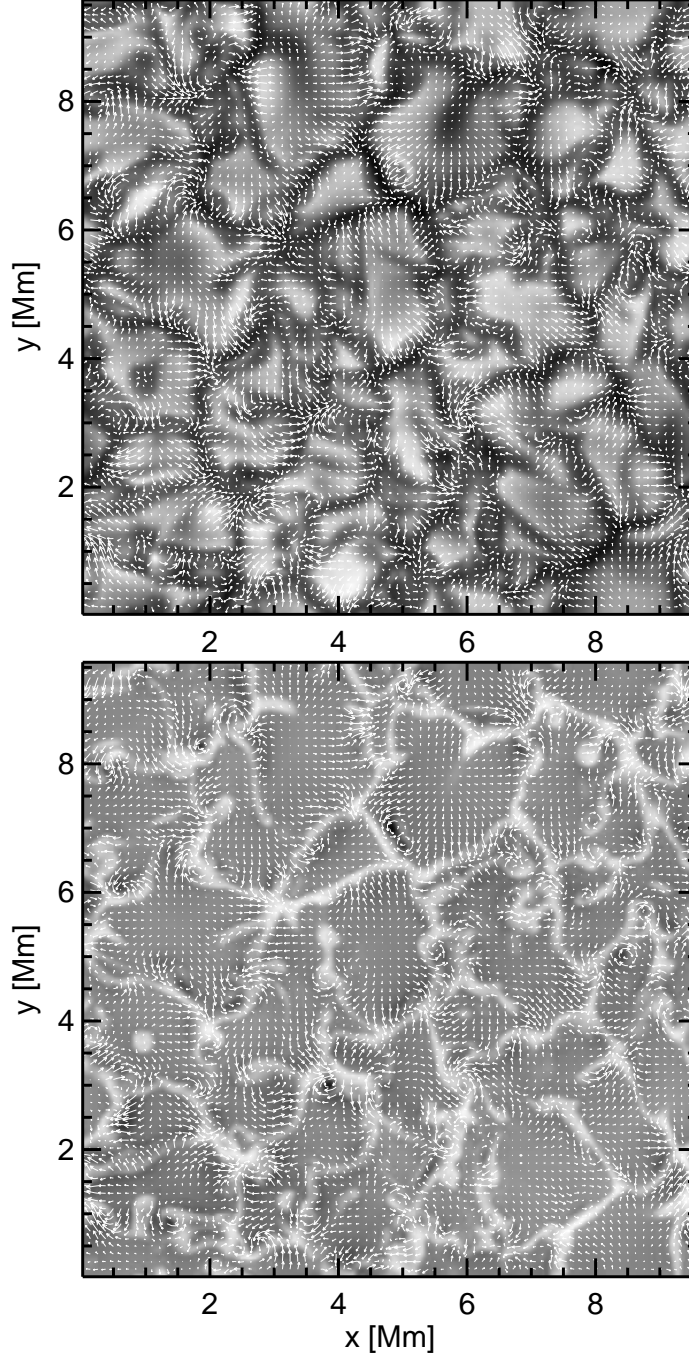


Figure 4. Top: Time instance of the bolometric intensity and the velocity field projected into the horizontal plane located at $\langle \tau_c \rangle = 1$. Bottom: Corresponding time instance of the logarithm of the density ($-6.25 \leq \log \rho \leq -6.86$) and the velocity field projected into the horizontal plane located 120 km below $\langle \tau_c \rangle = 1$. Under-dense vortices are visible at, e.g., $(x, y) = (3800, 3200)$ km, $(x, y) = (5000, 8500)$ km, $(x, y) = (1900, 8250)$ km, and twin swirls at $(x, y) = (5000, 7000)$ km. They have a density of typically 60% of the mean density. Intergranular lanes have typically 115%. The snapshot is from a magnetic field-free simulation with CO5BOLD.

2.4. Granular Lanes and Horizontal Vortex Tubes

It was known for long that in the visible continuum, the edges of granules tend to be brighter than the interior of granules or the intergranular space. High resolution observations have refined this knowledge. It was found that granules frequently show substructure in the form of lanes composed of a leading bright rim and a trailing dark edge, which form at the boundary of a granule and move together into the granule itself. Fig. 5 shows in the top row granules of the visible solar surface in fields of view of 5600×5600 km as observed with the SST and the Sunrise ballon-borne telescope. Events of granular lanes are marked with arrows. Simultaneously recorded Doppler maps (see Steiner et al. 2010) show that material flows in the upward direction within the bright granular lane with speeds of up to 1.8 km s^{-1} . Most of the area behind the bright rim, including the dark lane, harbors upflows as well but less strong, and sometimes even downflows. Close to the border of the granule and within the adjacent intergranular lane, the plasma flows in the downward direction with speeds up to 1.2 km s^{-1} .

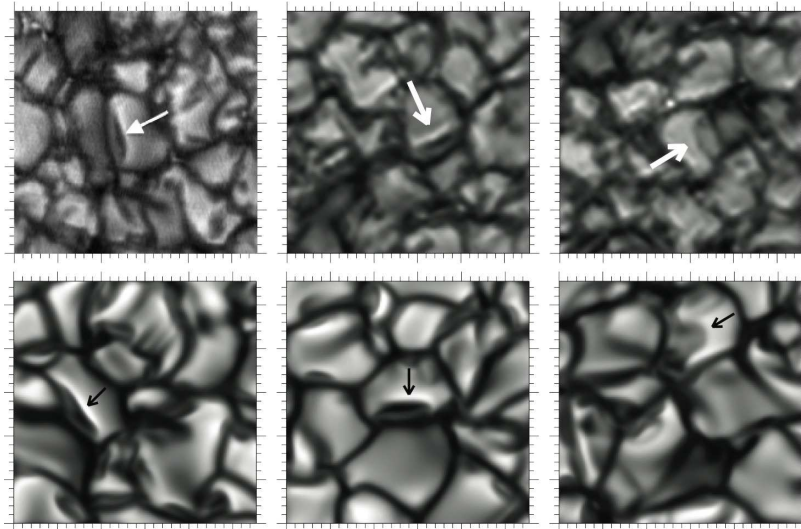


Figure 5. Top row: Granules of the visible solar surface in fields of view of approximately 5.6×5.6 Mm as observed with the SST (1st panel, courtesy L. Rouppe van der Voort) and the Sunrise ballon-borne telescope (2nd and 3rd panel). The threadlike, bright/dark stripes, marked with arrows, develop at the edge of a granule and move into the granule itself. Bottom row: Equivalent sections from an MHD simulation with the CO5BOLD code. The arrows mark strikingly similar threadlike objects, which prove to be vortex tubes. Adapted from Steiner et al. (2010).

The bottom row of Fig. 5 shows equivalent sections from a computer simulation. The arrows mark strikingly similar threadlike objects as are observed. From cross sections through the computational domain of the simulation, Steiner et al. (2010) conclude that these granular lanes are the visible signature of horizontally oriented vortex tubes. The axis of the vortex tube typically coincides with the trailing dark edge. Directly above the vortex tube, the flow assumes transonic speeds, roughly parallel to the solar surface. There, gas pressure and temperature are low, which opens a relatively transparent view to the cool interior of the vortex tube causing the dark edge. Rather than a proper movement, it is the shape and size of the vortex tube which changes in

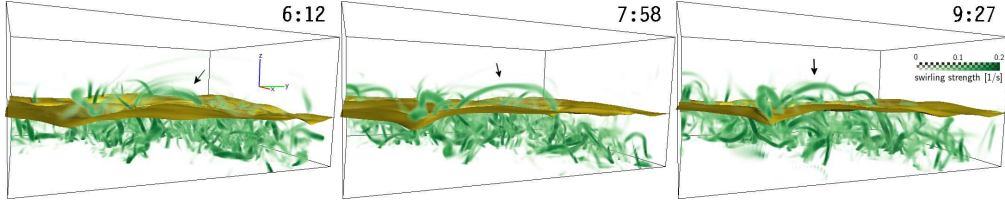


Figure 6. Rise and fall of a vortex arc. The plots display the swirling strength (green volume rendering) and the optical surface (yellow) at three different times (labels are in minutes). The size of the box shown is $1.5 \times 1.5 \times 0.8 \text{ Mm}^3$. Credit: Moll et al. (2011) reproduced with permission © ESO.

time and causes the horizontal displacement of the bright lane and the expansion of the trailing darkish area. In the simulation, we see occasional magnetic field intensification at locations of vortex tubes—one such case is shown in Steiner et al. (2011). Whenever magnetic fields are present, they tend to point in the horizontal direction near or above the $\tau_c = 1$ surface.

Yurchyshyn et al. (2011) observe that intergranular jets, originating in the intergranular space surrounding individual granules (Goode et al. 2010), tend to be associated with the formation and evolution of granular lanes. They speculate that the intergranular jets may result from the interaction of the turbulent small-scale fields associated with the vortex tube with preexisting larger-scale fields in the intergranular lanes. Since we found in Fig. 4 a singular case where twin whirlpools beneath the surface were an integral part of a granular lane, it cannot be excluded that sinkholes are an additional important ingredient for the production of the intergranular jets.

2.5. Small-Scale Vortices in Simulations of Solar Surface Convection

A synoptical view of small-scale vortices in simulations of solar surface convection was provided by Moll et al. (2011). These authors define the “swirling strength” based on an eigenanalysis of the velocity gradient tensor. It allows them to pick high-vorticity regions in which the plasma is swirling. The swirling regions form an unsteady network of highly tangled filaments, some of which protrude above the optical surface.

Near the optical surface, vertically oriented swirls are preferentially located within the intergranular lanes, where cooled fluid is sinking down in a turbulent fashion. Horizontal swirls are predominant at the edges of the granules. Above the optical surface, the three-dimensional structure of swirls is manifold, but often they appear in the form of bent and arc-shaped filaments as shown in Fig. 6. A similar type of structure was also reported by Stein & Nordlund (1998) and by Muthsam et al. (2010). Kitiashvili et al. (2012) discuss vortex tubes that reach into the chromosphere and interact with magnetic fields in their 3D simulations and they conclude that magnetized vortex tubes would effectively transfer energy and momentum from the photosphere to the chromosphere.

From Fig. 6, one can estimate that the arc-shaped swirl has a diameter of about 30 km, which is close to the grid size of 10 km of the numerical simulation. One could therefore speculate that in reality the swirling filaments would be even thinner. It would be extremely difficult to detect them with present day solar telescopes. Doppler-shift measurements have a depth resolution, limited by the formation width of the spectral line or a combination of spectral lines, which is definitively larger than 30 km.

3. The Horizontal Magnetic Field of Quiet Sun Regions

A fundamental achievement attained with Hinode's Solar Optical Telescope/Spectro-Polarimeter (SOT/SP) (Sakurai 2008) was the discovery that in the mean, the magnetic field over wide areas of the quiet Sun photosphere is predominantly horizontal (Lites et al. 2007, 2008; Orozco Suárez et al. 2007; Danilovic et al. 2010). From the analysis of time-averaged deep mode Stokes spectra with an effective integration time of 67.2 s and a noise level in the polarization continuum of about $2.9 \times 10^{-4} I_c$, Lites et al. (2008) came to the conclusion that the spatially averaged horizontal apparent flux density, as derived from wavelength-integrated measurements of the Zeeman-induced linear polarization, is 55 Mx cm^{-2} , five times more than the corresponding average vertical apparent flux density of 11 Mx cm^{-2} . This result, however, remained not undisputed.

3.1. Critiques of the Horizontal Field Measurements

Martínez González et al. (2008) analyzed spectro-polarimetric data of the Fe I lines at $1.5648 \mu\text{m}$ and $1.5652 \mu\text{m}$, recorded with the Tenerife Infrared Polarimeter (TIP) at the Vacuum Tower Telescope (VTT, Observatorio del Teide), of very quiet Sun regions at various heliocentric distances on the solar disk from $\mu = 1.0$ to $\mu = 0.28$. They restrict the analysis to profiles with a degree of polarization, $\sqrt{Q^2 + U^2 + V^2}$ larger than $4 \times 10^{-4} I_c$. They found that the circular and linear polarization amplitudes do not have any clear dependence on the heliocentric angle. This result points to an isotropic distribution of magnetic fields and is against any field topology with a preferred orientation within the field-of-view.

Beck & Rezaei (2009) observed a quiet Sun region at disk center with TIP@VTT, using the same lines as Martínez González et al. (2008). The noise level of the polarization signal was $2 \times 10^{-4} I_c$, where they set a threshold of $1 \times 10^{-3} I_c$ for the polarization degree during the analysis. They find that the total magnetic flux contained in the more inclined to horizontal fields ($\gamma > 45^\circ$) is about two times smaller than that of the less inclined fields. However, they do not conclude that this result would necessarily contradict the results of Lites et al. because of the different formation heights of the lines at $1.56 \mu\text{m}$ and at 630.2 nm . In fact, simulations (Schüssler & Vögler 2008; Steiner et al. 2008; Danilovic et al. 2010) show a strong height dependence of the horizontal magnetic field—while the vertical component may dominate in the deep photosphere, the horizontal component becomes important in the upper photosphere and lower chromosphere only. Beck & Rezaei (2009) also emphasize that the pixel to pixel variation of the thermal structure of the atmosphere should be properly taken into account during the analysis of the polarization signal. This is not taken into account when using a global (pixel independent) calibration curve for the derivation of magnetic field strengths as was done by Lites et al.

Asensio Ramos (2009) carried out a Bayesian analysis of the ‘normal mode’ data (4.8 s exposure time, $\sigma_{\text{noise}} \approx 1.2 \times 10^{-3} I_c$) of Lites et al. (2008). He points out that the noise level present in the Hinode SOT/SP observations induces a substantial loss of information for constraining the angular distribution of the magnetic field. However, the results indicate that the field of pixels with small polarimetric signals has a quasi-isotropic distribution. He also finds that the magnetic field strength in the internetwork region is clearly in the hectogauss regime with 95% confidence.

Table 2. Angular distribution of the internetwork magnetic field as determined by various authors. The entries in the column ‘angular distribution’ must be considered an over-all summary, the details being more complex. A pure isotropic angular distribution would lead to $\langle B_{\text{app}}^T \rangle / \langle B_{\text{app}}^L \rangle = \pi/2$. The entries in the lower part of the table refer to numerical simulations, for which the ratio $\langle B_{\text{app}}^T \rangle / \langle B_{\text{app}}^L \rangle$ was derived from synthesized Stokes profiles and application of a PSF corresponding to that of Hinode/SOT. Numbers in parentheses without PSF.

no.	authors	instrument/ simulation	line [nm]	angular distribution	$\langle B_{\text{app}}^T \rangle /$ $\langle B_{\text{app}}^L \rangle$
1	Lites et al. (2007, 2008)	SOT/SP	630	predominantly horizontal	5
2	Orozco Suárez et al. (2007)	SOT/SP	630	predominantly horizontal	2.1
3	Martínez González et al. (2008)	VTT/TIP	1560	isotropic distribution	—
4	Beck & Rezaei (2009)	VTT/TIP	1560	predominantly vertical	0.42
5	Asensio Ramos (2009)	SOT/SP	630	isotropic for weak fields	—
6	Danilovic et al. (2010)	SOT/SP	630	predominantly horizontal	5.8
7	Stenflo (2010)	SOT/SP	630	predominantly vertical	—
8	Ishikawa & Tsuneta (2011)	SOT/SP	630	predominantly vertical	0.86
9	Borrero & Kobel (2011)	SOT/SP	630	undeterminable	—
10	Borrero & Kobel (2012)	SOT/SP	630	non-isotropic	—
11	Steiner et al. (2008)	h20	630	predominantly hor-	4.3 (2.8)
		v10	630	izontal	1.6 (1.5)
12	Danilovic et al. (2010)	C mf=3	630	predominantly hor-	9.8 (3.5)
		C+B _{ver}	630	izontal	4.2 (2.6)

Yet another way of analyzing the Hinode SOT/SP data was advanced by Stenflo (2010). He carried out a thorough analysis of the ratio of the amplitudes of the blue wing of Stokes V of Fe I $\lambda\lambda$ 630.15 and 630.25 nm and finds a “magnetic dichotomy” with two distinct populations, representing strong (kG) and weak fields. With regard to the inclination he finds that the angular distribution is extremely peaked around the vertical direction for the largest flux densities, but gradually broadens for smaller flux densities, to become asymptotically isotropic at zero flux density. This means that the magnetic field has a predominantly vertical orientation, quite opposite to the findings of Lites et al. (2007, 2008) and Orozco Suárez et al. (2007). We come back to Stenflo’s method in Sect. 3.4.

Ishikawa & Tsuneta (2011) find, based on Hinode SOT/SP data, a clear positional association between the vertical and the horizontal magnetic fields in the internetwork region. Essentially, all of the horizontal magnetic patches are associated with vertical magnetic patches and half of the vertical magnetic patches are associated with horizontal magnetic patches. This points to small-scale magnetic loops with bipolar footpoints, and to canopy fields of magnetic flux concentrations as an important source of the horizontal magnetic field. In fact, tiny emerging loops of granular and sub-granular scale were observed with SOT/SP by Ishikawa et al. (2010) and Martínez González et al. (2010). Steiner et al. (2008) show an example of an emerging sub-granular horizontal field patch framed by opposite polarity footpoints of vertical field from their simulations. They describe it as a consequence of convective overshooting, which transports horizontal fields into the photosphere. Schüssler & Vögler (2008) see the loopy structure of the small scale magnetic field in the photosphere as a direct outcome of the

surface dynamo which operates in the surface layers of the convection zone (see also Steiner (2010) for a sketch explaining why such a loopy structure leads to an increasing dominance of the horizontal field component with increasing height in the atmosphere). Prior to this, Lites et al. (1996) report isolated, predominantly horizontal magnetic flux patches of $1''$ – $2''$ and smaller size, often occurring between regions of weak opposite polarity Stokes V profiles, which they suggested to be the emergence of small, concentrated loops of magnetic flux.

Ishikawa & Tsuneta (2011) measure for an internetwork region a mean longitudinal (vertical) magnetic flux density of 8.3 Mx cm^{-2} and a mean transverse (horizontal) flux density of 7.1 Mx cm^{-2} , thus a clear dominance of the vertical fields. Note that while the former number is close to the value obtained by Lites et al. (2007, 2008) and Orozco Suárez et al. (2007), the latter is about 8 times smaller. One reason for this discrepancy is the stringent noise criteria that was applied to the data by Ishikawa & Tsuneta (2011). Since a transversal field produces a much weaker signal in linear polarization than a longitudinal field of equal strength in circular polarization, there is a bias towards longitudinal fields when applying a common noise level and discarding any signal below it. Correspondingly, Ishikawa & Tsuneta (2011) find only 10.1% of a supergranular cell sized subfield having sufficient linear polarization for entering the analysis, while 43.8% have sufficient circular polarization. On the other hand applying no noise level gives preference to transversal fields because pure noise would produce spurious large amounts of transversal field. We come back to the problem of selection effects in Sect. 3.3.

Table 2 provides an overview of the above discussed various attempts to determine the horizontal vs. the vertical mean flux density (or the angular distribution) of the internetwork magnetic field.

3.2. The Photon-Noise Problem

The main reason for the disparate results highlighted in Table 2 is due to the different sensitivity of linear and circular polarization to magnetic fields, in combination with the finite sensitivity of the measurements due to photon noise. The problem was nicely demonstrated and discussed by Borrero & Kobel (2011). In order to test if it was actually possible to accurately retrieve the magnetic field vector employing the Fe I line pair at 630 nm in regions with very low polarization signals such as in internetwork regions, Borrero & Kobel (2011) carried out several Monte-Carlo simulations with synthetic data. They start from a map of magnetic field vectors and associated atmospheric parameters, which they obtained in the first place from a Stokes inversion of real SOT/SP data. Then, they arbitrarily set the transversal magnetic field to zero, synthesize the Stokes profiles from this map and add different amounts of noise. Then they invert these data back to magnetic field vectors as if they were actually observational data. Clearly, the subsequent inversion should result in zero transversal field. However, this is not the case as is shown in Fig. 7.

The four panels show the results for different amounts of noise that was added to the synthesized profiles—from $1.0 \times 10^{-3} I_c$ (top left) to $1.0 \times 10^{-5} I_c$ (bottom right). $2.8 \times 10^{-4} I_c$ corresponds to the noise level of the least noisy SOT/SP data used by Lites et al. (2007, 2008). The inversion procedure asks for a threshold of the signal to noise ratio. When either Stokes Q , U , or V are above this noise level, the pixel is considered for inversion. This ratio was taken 3, 4.5, and 6, but the different curves corresponding to these values are almost identical. The curves are histograms of the

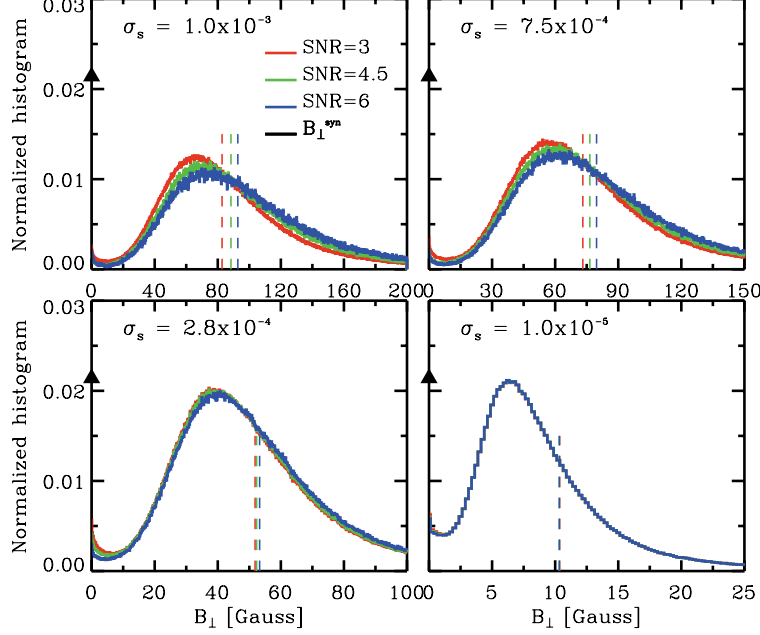


Figure 7. Histograms of the transverse component of the magnetic field, B_{\perp} , which is purely induced by different levels of noise, σ_s , indicated in the top left of each panel. The different curves correspond to different signal-to-noise threshold for a pixel to be considered for inversion. The vertical black arrow indicates the δ -Dirac distribution of the true, original transverse component. The vertical, dashed lines indicate the center of gravity of the histograms. Credit: Borrero & Kobel (2011) reproduced with permission © ESO.

transversal magnetic flux density and should really be δ -Dirac distributions centered at zero if the inversion was correct. However, the center of gravity of the histograms (indicated by the vertical dashed lines) is 80–90 G for a noise level of $1.0 \times 10^{-3} I_c$ and close to 55 G for the noise level of $2.8 \times 10^{-4} I_c$, which is, coincidence or not, the value for the mean transversal apparent flux density determined by Lites et al. (2007, 2008). Even at a hypothetical noise level of $1.0 \times 10^{-5} I_c$, the retrieved histogram of the transversal field still has a center of gravity of 10 G and peaks at about 6 G instead of 0 G.

Here is a note in place. The signal to noise limits used here refer to single wavelength points, not to integral quantities like $Q_{\text{tot}} = \int_{\lambda_b}^{\lambda_r} Q(\lambda) d\lambda / I_c \int_{\lambda_b}^{\lambda_r}$. Thus, even though the probability that photon noise produces a signal above 3σ , at a given wavelength position, is only 0.3%, it is almost guaranteed that one of the 112 wavelength points in either Stokes Q , U , or V surpasses this limit and therefore the full profiles enter the analysis. Thus, even with a signal to noise ratio of 5, there are still ample profiles that enter the analysis with linear polarization that is interpreted as real although it would be strictly zero without the addition of noise. Also, most of these profiles are chosen because at least one of the wavelength points in Stokes- V surpasses the signal-to-noise limit and none in Stokes Q or U . This then leads for example in the case of $\sigma = 2.8 \times 10^{-4} I_c$ to a residual horizontal field strength of 55 G, much more than the corresponding vertical field strength, which in this case is around 20 G and therefore,

the field would be interpreted as predominantly horizontal although it is strictly vertical in reality. This devastating result sheds serious doubts on previous determinations of the angular distribution of internetwork magnetic fields based on Stokes inversion methods.

In defense of the work of Lites et al. (2007, 2008) it should be noted however that they worked exclusively with integral quantities, V_{tot} and L_{tot} , which should be much less affected by noise. However this forced them to use a previously determined calibration curve for the conversion of total linear and total circular polarization into field strength. This calibration was derived from a given atmosphere and therefore it cannot take pixel to pixel variation of the atmospheric parameters into account, which was found to be important by Beck & Rezaei (2009). Also, Lites et al. did not use Stokes Q and U separately, but tried to determine the “preferred-frame azimuth” for each pixel so that Stokes U vanishes, enhancing the signal in Stokes Q . This procedure should enhance the signal to noise in linear polarization but is of course itself subject to noise. Danilovic et al. (2010) applied Lites et al.’s method to white noise with a level of $\sigma = 8 \times 10^{-4} I_c$ and obtained a mean spurious transversal magnetic field strength of 36 G, which is about half of what is shown for a similar noise level in Fig. 7, indicating that Lites et al.’s method produces considerably less spurious horizontal field than straightforward Stokes inversion does.

3.3. Selection Effects

There are different ways of selecting pixels as having good enough signal for a trustworthy determination of the magnetic field vector, all leading to biases in one or the other way, again due to the largely different sensitivity of the circular and linear polarization to magnetic fields.

Selecting pixels only which have either Stokes V or Q or U above the noise level gives a strong bias towards horizontal fields. This is because most pixels will be selected because they have a Stokes V above the noise level (because of the high sensitivity of Stokes V to longitudinal fields) but these pixels are dominated by noise in Stokes Q and U , which then will yield substantial amounts of false transversal field (because of the low sensitivity of linear polarization to transversal fields).

One could think that the obvious remedy consists in selecting pixels only that have signals in Stokes V and Q or U ($V \wedge (Q \vee U)$) above the noise level. However, this again gives preference to horizontal fields because in this case only pixels with strong transversal fields are chosen, while the many pixels with Stokes V above the noise level and Q or U below it are discarded.

One way (which has not been tried out so far) to circumvent these problems would consist in setting limits in the real physical space of field strengths, instead of in the Stokes space. Thus, we demand that either B_{\parallel} or B_{\perp} be larger or equal to a given field-strength limit B_{lim} . Then,

$$V_{\text{lim}} = c_c B_{\text{lim}} \quad \text{and} \quad Q_{\text{lim}} = c_l^2 B_{\text{lim}}^2, \quad (2)$$

where we now work without loss of generality in the preferred-frame azimuth where U vanishes. c_c and c_l are calibration constants that could possibly vary from pixel to pixel. Then

$$\frac{V_{\text{lim}}}{c_c} = B_{\text{lim}} = \sqrt{\frac{Q_{\text{lim}}}{c_l^2}} = \frac{1}{c_l} \sqrt{n\sigma_{\text{noise}}}, \quad (3)$$

where we now demand that Stokes Q be $n\sigma_{\text{noise}}$ above the noise level if it is to be used for determining the transversal field. This then leads to the selection criterium

$$Q \geq n\sigma_{\text{noise}} \quad \text{or} \quad V \geq \frac{c_c}{c_l} \sqrt{n\sigma_{\text{noise}}} . \quad (4)$$

Note that the criterium for Stokes V is much more stringent than that for Q , which is expression of setting equal lower field-strength limits to the transversal and longitudinal field. Still, we expect many pixels to satisfy the stringent criterium for Stokes V but still not the less stringent criterium for Stokes Q . In this case we propose to discard Q , assuming the field to be strictly vertical. On the other hand in the rare case where Q satisfy the criterium but not V , we consider the field as strictly horizontal. In case where both Q and V satisfy their individual criterium, the magnetic field vector can be determined.

These criteria should remedy the one-sided preference for horizontal fields but still has its own problems. It can be expected to give some preference to strictly vertical and strictly horizontal fields. Also, large amounts of pixels that would have a V signal above $n\sigma_{\text{noise}}$ are discarded for inversion because they do not fulfill the more stringent criterium for V , Eq. 4. Therefore, for only a fraction of a given polarization map the magnetic field could be retrieved, making it difficult to reliably determine mean values of transversal and longitudinal flux over the full map.

3.4. Stokes-V Amplitude Ratios

There are, roughly speaking, two ways of retrieving the magnetic field vector from polarimetric data. With the *Stokes inversion* procedure one starts with a given atmospheric model including a magnetic field, computes the Stokes profiles of one or several spectral lines by solving the Unno-Rachkowsky equations of polarized radiative transfer in a forward fashion, and compares them to the observed ones. Then, the magnetic field vector, thermal atmospheric structure, line-of-sight velocity, magnetic filling factor, and possibly the micro and macro turbulence parameters and stray-light contributions are iteratively adjusted until a satisfactory agreement between synthesized and observed profiles is achieved. The first such automatic Stokes inversion code was described in Keller et al. (1990). This procedure is repeated pixel by pixel of a polarimetric map, so that the atmospheric parameters are allowed to vary, say from the interior of a granule to the intergranular lane. Stokes inversion procedures were chosen by the authors of the second, fourth, fifth, and ninth row of Table 2. In a sense, it can be considered the classical way of atmospheric modeling as is performed in deriving standard stellar model atmospheres.

Many solar physicist distrust Stokes inversion procedures because of the many free parameters that need to be adjusted (which renders the solution non-unique), the potential vulnerability to noise, and the relatively complex programs, which give the impression of black boxes (see Ruiz Cobo (2007) for replies to such concerns). Instead, they take resort in simple procedures derived from first principles of spectro-polarimetric line formation theory. This approach may allow them to work with spectrally integrated quantities, like V_{tot} and L_{tot} mentioned in Sect. 3.2, which may be less susceptible to noise. However, such basic receipts invariably end up in using a calibration curve for converting Stokes signals to magnetic field strengths. Usually, the calibration applies globally so that no pixel to pixel variation in the thermodynamic variables is taken into account. Such procedures were chosen by the authors of the first and sixth to eighth

row of Table 2. The synthetic data of rows 11 and 12 were inverted with Lites et al.’s method. Of course, also this second, more fundamental way of deriving the magnetic field vector can be considered a Stokes inversion procedure—one is tempted to call it a “poor man’s inversion procedure”. Its advantage is that it immediately derives from the observed data and its model dependency is less complex.

One method on this second route for retrieving the true magnetic field strength of quiet Sun regions consists in considering the Stokes- V amplitude ratio of two spectral lines. Traditionally, this was done with the two lines Fe I $\lambda\lambda$ 525.022 and 524.706 nm, which yield the so called magnetic line ratio (Stenflo 1973). The two lines have effective Landé factors 3.0 and 2.0, respectively, but are otherwise identical in terms of line strength and excitation potential and belong to the same atomic multiplet. Therefore, the two lines behave virtually identical with regard to formation height and thermal response but they vary in the sensitivity to magnetic fields.

In the weak field regime in which the Zeeman splitting is much smaller than the width of the spectral line (at most a few hundred Gauss),

$$V(\lambda) \propto g \frac{\partial I(\lambda)}{\partial \lambda}, \quad (5)$$

where $V(\lambda)$ is the Stokes V profile, the difference between left and right circularly polarized intensity and $I(\lambda)$ the Stokes I profile, the regular, natural light intensity (absorption profile). g is the effective Landé factor. Equation (5) simply derives from the leading term of the Taylor expansion of the two Zeeman components expressed in terms of the I profile (see e.g. Stenflo 1994, chapter 12.2). Then the Stokes V ratio of two lines 1 and 2 is

$$\frac{V_1}{V_2} = \frac{g_1}{g_2} \frac{\partial I_1 / \partial \lambda}{\partial I_2 / \partial \lambda} \approx \frac{g_1}{g_2}, \quad (6)$$

which is in particular also valid for the wavelength position where Stokes V assumes its peak value. The second relation of Eq. (6) is well satisfied only when lines 1 and 2 are virtually identical and form under very similar conditions as is the case for the line pair Fe I $\lambda\lambda$ 525.022 and 524.706 nm. As long as the magnetic field is intrinsically weak, the Stokes- V amplitude-ratio is g_1/g_2 . But with increasing field strength, the Stokes- V amplitude starts to saturate, first the line with the larger g -factor while the V amplitude of the line with the smaller g -factor continues to grow and Eq. (6) breaks down because higher order terms in the above mentioned Taylor expansion come into play. At field strength in the order of 1 kG, the two amplitudes are of similar size, meaning that the amplitude ratio approaches $V_1/V_2 \approx 1$. Further increase of the magnetic field strength merely increases the Zeeman splitting between the blue and the red lobe of the Stokes profile, linearly with field strength. Thus, the line-ratio method provides an easy and comprehensible tool for differentiating between weak and strong fields in the regime where full Zeeman splitting of the lines has not yet taken place, making it possible to dispense with detailed radiation transfer and modeling. It is important to notice that the line-ratio method also works when only a small fraction of the spatial resolution element is occupied by magnetic fields (small filling factor) so that the method yields information about sub-resolution magnetic fields, i.e., the *intrinsic* field strength.

Unfortunately, Hinode SOT/SP does not detect the ideal line pair Fe I $\lambda\lambda$ 525.022 and 524.706 nm but instead the line pair Fe I $\lambda\lambda$ 630.151 and 630.250 nm with respective Landé factors 1.667 and 2.5, for which the second relation of Eq. (6) is less well satisfied because the ratio of Stokes- I derivatives does not cancel out but introduces an intricate dependence on temperature and velocity in the atmosphere (Khomenko & Collados

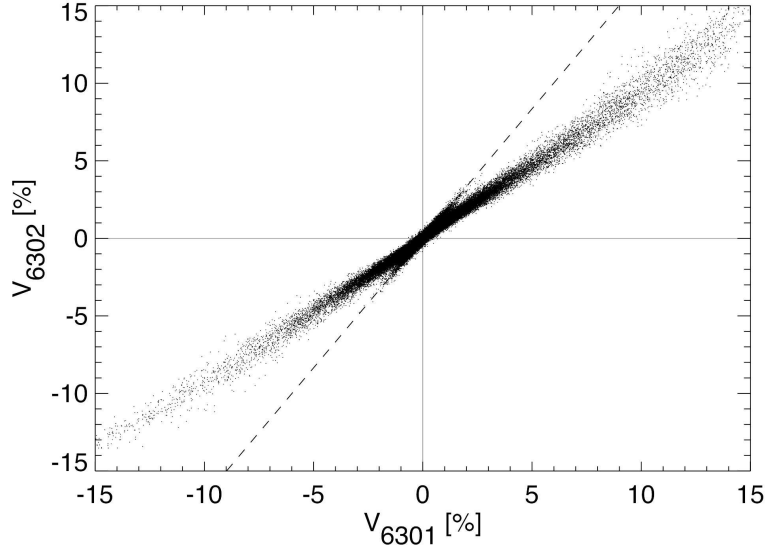


Figure 8. Scatter plot of the blue lobe Stokes- V amplitude of Fe I 630.250 nm vs. the corresponding amplitude of Fe I 630.151 nm from the leftmost third of the ‘normal mode’ map shown in Figs. 1 and 2 of Lites et al. (2008). The dashed line with slope $s = 1.66$ represents the regression relation that would be expected for intrinsically weak fields. Note the two populations of points: (1) The dominant population that follows a slope of about $0.65s$ for small polarizations. (2) A secondary population of Stokes V amplitudes below about 2%, which closely follows the dashed line. The method for determining the Stokes- V amplitudes was the same as used by Stenflo (2010) (Fig. 8) for a different (‘deep mode’) data set.

2007). Therefore it did not seem advisable to apply the line-ratio method to SOT/SP data. Nevertheless, Stenflo (2010) gave it a try, which led him to a remarkable discovery which is displayed in Fig. 8.

Fig. 8 shows a scatter plot of the blue lobe Stokes- V amplitude of Fe I 630.250 nm vs. the corresponding amplitude of Fe I 630.151 nm for a SOT/SP “normal mode” data set recorded at quiet Sun disk-center, viz., the leftmost 100'' of the map shown in Figs. 1 and 2 in Lites et al. (2008). Fig. 8 is from a different dataset than, but very similar to Fig. 8 of Stenflo (2010) and the Stokes- V amplitudes were determined with the same method as described in Stenflo (2010). The dashed line with slope $s = 1.66$ represents the regression relation that would be expected for intrinsically weak fields. It is close to the ratio of the respective Landé factors, $g_{630.25}/g_{630.15} = 2.5/1.667 = 1.5$ but not exactly because the ratio of the derivatives in Eq. (6) is not unity but rather 1.1 at the wavelength position of maximum Stokes V amplitude of the blue lobe. The unexpected result is that there exists two populations of points: (1) The dominant population that follows a slope that is about $0.65s$ for small polarizations, decreasing to about $0.55s$ for larger values. (2) A secondary population that is significant only for Stokes V amplitudes below about 2%, and which closely follows the dashed line. Even at the 1% polarization level, the two components can be clearly separated when plotting the histogram of the points in a bin around this polarization level (Stenflo 2010, Fig. 9). Reliable decompositions are found down to $V_{630.15} \gtrsim 0.6\%$.

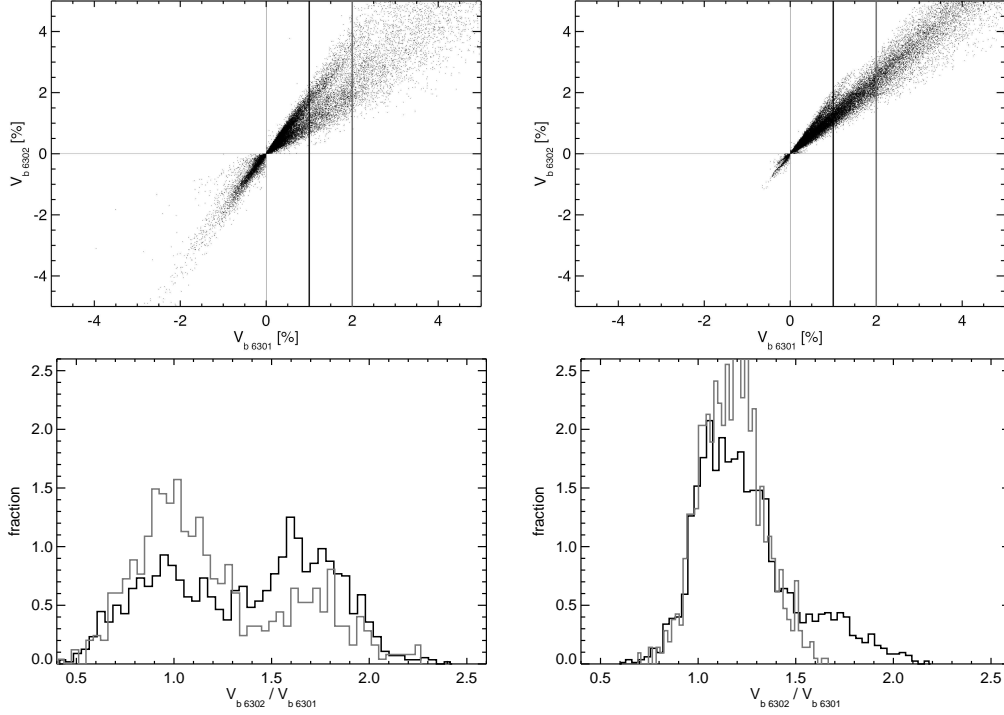


Figure 9. Top row: Scatter plot of the Stokes- V amplitude of the blue lobe of Fe I 630.250 nm vs. the corresponding amplitude of Fe I 630.151 nm of synthesized V profiles from the CO5BOLD MHD simulation v50. The scatter to the left is from pixels at full spatial resolution, the scatter to the right from the same data after application of the SOT PSF. The vertical lines indicate the polarization levels which the histograms in the bottom row correspond to. Bottom row: Histograms of the points that fall within the range $0.8 \leq V_{630.15} \leq 1.0$ (black) and $1.8 \leq V_{630.15} \leq 2.0$ (gray).

Fig. 8 has a simple and elegant explanation in terms of the Stokes- V line-ratio theory. Clearly, the points of the second population must correspond to intrinsically weak fields because their Stokes- V amplitude ratios are in close agreement with the weak field limit (dashed regression relation). The points of the first population must correspond to kG fields because their Stokes- V amplitude ratios is approaching, and even dropping below, one, which points to strong fields as explained above. But how is it possible that the strong field component exists not only for large polarization amplitudes, which may stem from network elements, but extends down to very small polarization levels? One would rather expect the scatter plot to display a S-shape—the inner part being occupied by the weak field component with slope $s \approx 1.66$ and the outer part by the strong field component with slope $s \approx 1.1$. The answer to this question is filling factor. There must exist ample amounts of kG-fields of sub-resolution size (small magnetic filling factor), which give only weak polarization amplitudes but nevertheless betray themselves as being intrinsically strong because of a small Stokes- V amplitude ratio. Thus, pixels with polarization levels around and below 1% must harbor kG flux concentrations of very small size and in fact, Stenflo (2011) deduces from these results kG flux tubes with diameters down to 10 km. As elegant and obvious this explanation of Fig. 8 may appear, caution is indicated as is demonstrated in the following.

3.5. Stokes- V Amplitude Ratios from Simulations

Fig. 9 shows the inner part of a scatter plot of the same quantities as shown in Fig. 8 but of Stokes- V profiles that were synthesized from the CO5BOLD MHD-simulation v50 referred to in Sect. 2.3. The top left panel shows the scatter plot from the data at full spatial resolution, the top right panel after application of the Hinode/SOT point spread function (PSF) of Wedemeyer-Böhm (2008) to the full resolution data. Here, we do not use Stenflo’s fitting method for determining the Stokes- V amplitudes but take the actual amplitude, discarding abnormal Stokes- V profiles. The bottom panels show the corresponding histograms of the points that fall within the range $0.8 \leq V_{630.15} \leq 1.0$ (black) and $1.8 \leq V_{630.15} \leq 2.0$ (gray), again, once from the full resolution data (left) and once from the data after application of the SOT PSF (right). We see immediately that, like in the real, observed data, there are two populations of points: (1) The dominant population that follows a slope that is about 0.6s. (2) A secondary population that is significant only for Stokes V amplitudes below roughly 2%, and which approximately follows a regression line with slope $s = 1.66$. For the full resolution data, even at the 1% polarization level, the two components can be clearly separated as can be seen from the two distinct humps in the corresponding histogram.

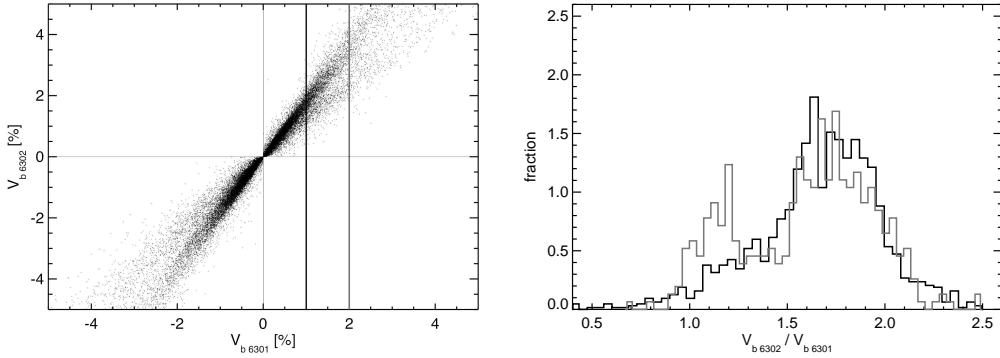


Figure 10. Left: Scatter plot of the blue lobe Stokes- V amplitude of Fe I 630.250 nm vs. the corresponding amplitude of Fe I 630.151 nm of synthesized V profiles from the CO5BOLD MHD simulation h50. The scatter is from pixels at full spatial resolution. Right: Corresponding histogram of the points that fall within the range $0.8 \leq V_{630.15} \leq 1.0$ (black) and $1.8 \leq V_{630.15} \leq 2.0$ (gray).

A scatter plot from a snapshot of the simulation h50 (Fig. 10) shows a similar behavior with the difference that both polarities are equally represented and that the weak field population is now the major one. This is because in this simulation the field is weaker and more turbulent than in simulation v50 and has no preferred polarity from the beginning.

On the background of the explanation for the observed scatter plot in terms of intrinsically weak and strong fields and in terms of the magnetic filling factor, the result from the synthesized data is very surprising. Since the simulations cannot harbor any sub-resolution magnetic elements because there cannot be any structure smaller than the resolution limit given by the computational grid, the magnetic area filling factor for a single computational cell is always one, irrespective of the field strength. Thus, the argument that pixels of small polarization degree with a Stokes- V line-ratio in the order of unity must origin from kG flux concentrations of small filling factor cannot apply to

the simulation data. For those, the two populations of points in the scatter plot must have a different origin.

3.6. Interpretation of the Simulation Data

On the one hand side, it is reassuring that the MHD simulations reproduce the observed two populations of points in scatter plots of the Stokes- V amplitudes of the lines Fe I $\lambda\lambda$ 630.151 and 630.250 nm. On the other hand, we found in Sect. 3.5 that the two populations cannot be explained in terms of the very attractive and elegant hypothesis put forward by Stenflo (2010) of a “magnetic dichotomy” with two distinct populations representing strong (kG) and weak fields, or “collapsed” and “uncollapsed” fields as he expresses it. The question then is, what causes the two populations if not the dichotomy of “collapsed” and “uncollapsed” fields?

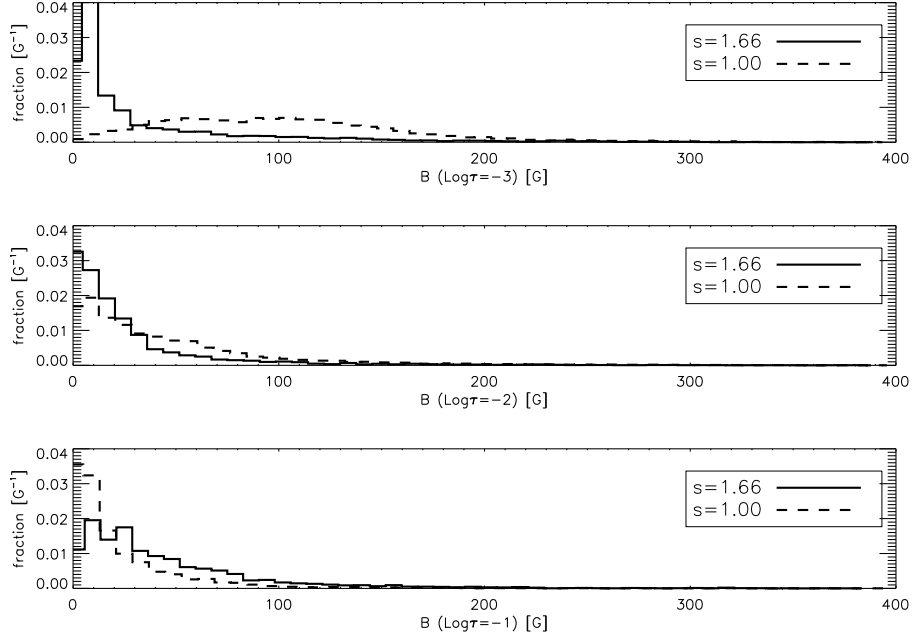


Figure 11. Histograms of the absolute magnetic field strength at three different optical depth levels $\log \tau = -3$ (top), -2 (middle), and -1 (bottom), for the points of the full resolution scatter plot of Fig. 9 with a polarization level of $1.0 \leq V_{630.15} \leq 2.0$. Dashed curve: Histograms of the main population of points with Stokes- V amplitude ratio $V_{630.25}^b / V_{630.15}^b \leq 1.5$. Solid curve: Histogram of the population with Stokes- V amplitude ratio $V_{630.25}^b / V_{630.15}^b \geq 1.5$.

Figure 11 partially answers this question. It shows the histograms of the absolute magnetic field strength at three different optical depth levels $\log \tau = -3$ to -1 for the points of the full resolution scatter-plot of Fig. 9 with a polarization level of $1.0 \leq V_{630.15} \leq 2.0$. Each panel contains two histograms: one for the main population of points with Stokes- V line-ratio $V_{630.25}^b / V_{630.15}^b \leq 1.5$ (dashed) and one for the population of points with Stokes- V line-ratio $V_{630.25}^b / V_{630.15}^b \geq 1.5$ (solid). The second population should correspond to intrinsically weak magnetic fields because they cluster around a Stokes- V amplitude ratio of 1.6, which is the value in agreement with the weak

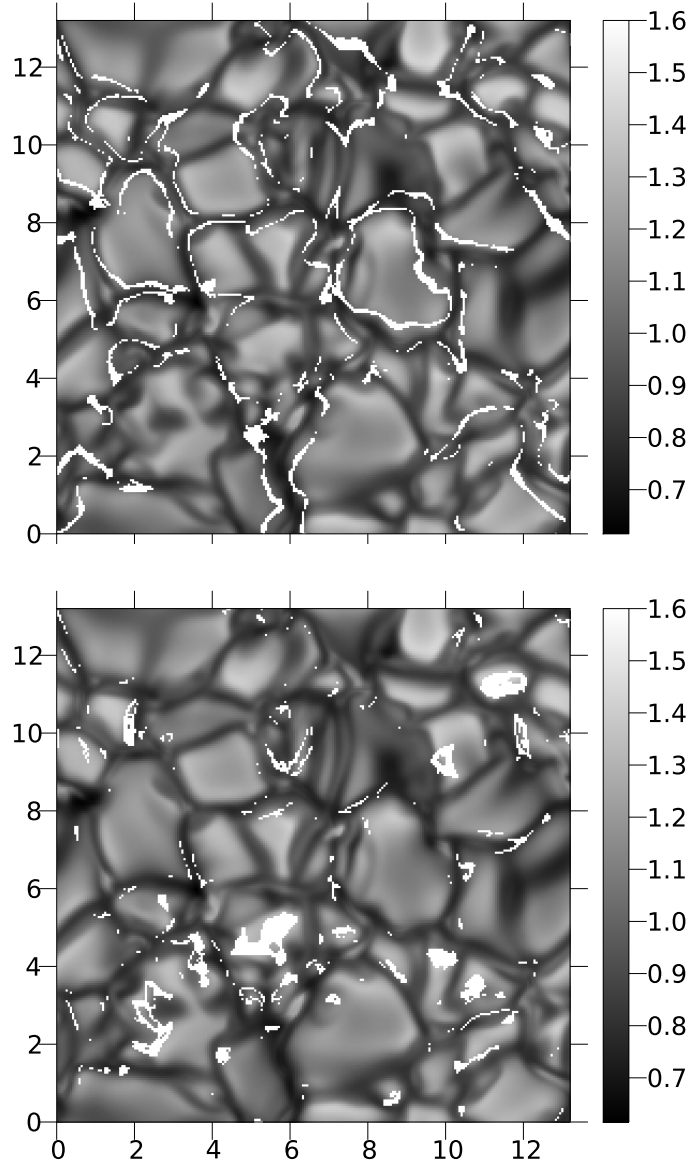


Figure 12. Top: Location of pixels (white) with a polarization level $1.0 \leq V_{630.15} \leq 2.0$ belonging to the population of pixels with $V_{630.25}^b/V_{630.15}^b \leq 1.5$ (first, main population). Bottom: Location of pixels with a polarization level $1.0 \leq V_{630.15} \leq 2.0$ belonging to the population with $V_{630.25}^b/V_{630.15}^b \geq 1.5$ (second, intrinsic weak field population). Background: Continuum intensity at 630 nm.

field approximation. In fact, we can see from the histograms that this is true: the field strength for this population stays essentially below 200 G with a peak at 10 G. But we also see that the first population that should correspond to “collapsed” kG flux concentrations is weak field as well with field strengths mostly below 300 G. There is however a distinct difference with respect to the second population: the peak and bulk of the histogram shifts to higher field strengths with height in the atmosphere. This means that for this population of points, the magnetic field strength increases with height in the atmosphere, which is opposite to the usual case.

When plotting the histogram of the magnetic field inclination with respect to the vertical direction (not shown here) we see that the first population shows mainly horizontal fields in the deep layers, which become inclined by $\approx 45^\circ$ at $\log \tau = -2$ to -3 when the field strength increases. This behavior points towards canopy magnetic fields as the origin of this, formerly called, the “collapsed” (Stenflo 2010) component. Canopy fields may stem from magnetic flux concentrations in the photosphere, which expand and fan out in the lateral direction with increasing height in the atmosphere (Steiner 2000). The magnetic field along a line of sight that traverses the canopy field is weak in the optically deep layers below the canopy but abruptly increases in strength and assumes a large inclination angle at the transition from below to within the canopy. Another indication that points to canopy fields comes from the histograms of the vertical velocity, which show mainly upflows at all optical depth levels for the second, intrinsically weak field population, but downflows in the deepest layer of the first population. This can be expected because canopy fields are most likely found in the vicinity of (vertical) magnetic flux concentrations which in turn are found within intergranular lanes, which harbor downflows. Therefore, we expect canopy fields and hence, pixels belonging to the first population, to exist at the border between intergranular lanes and granules with a tendency of having downflows in the deep layers.

Figure 12 confirms that this is indeed the case. The top panel shows on the background of the continuum intensity at 630 nm the location of pixels that have a polarization level $1.0 \leq V_{630,15} \leq 2.0$ and belong to the first population with $V_{630,25}^b/V_{630,15}^b \leq 1.5$. Clearly, these pixels are found along the boundaries of granules, where canopy fields exist. The bottom panel shows the pixels belonging to the second population with $V_{630,25}^b/V_{630,15}^b \geq 1.5$. These pixels occur in patches within granules and are mainly associated with horizontal field, which is probably transported into the photosphere by instances of granular overshooting.

From all this we conclude that the two population of pixels with low polarization amplitudes found in data of synthesized Stokes- V profiles of magneto-convection simulations are *not* due to a dichotomy between “collapsed” and “uncollapsed” fields, but to a distinct difference between profiles from granule interiors and profiles from the boundary region between granules and the intergranular space. Truly strong fields are found within the intergranular lane proper but they have a larger polarization degree and therefore pertain to the outskirts of the line-ratio scatter-plots. It is very likely, that this explanation of the two populations also holds for the observed Stokes- V profiles. This then means that there is no need for the introduction of collapse sub-resolution flux-concentrations, and that the conclusions of Stenflo (2010) that the inter-network magnetic field was predominantly vertical is premature because of its shaky premises.

3.7. The Horizontal Field from Numerical Simulations

From the critiques reviewed in Sects. 3.1 and 3.2 it is clear that the angular distribution of the magnetic field in network-cell interiors has not yet been reliably measured. It is not even clear if there exists indeed a predominance of the horizontal field component. The analysis of Lites et al. (2007, 2008), which uses and derives least noise affected data, points in this direction. On the other hand, numerical MHD simulations of the solar surface layers have resulted in a predominance of the horizontal fields (Grossmann-Doerth et al. 1998; Abbett 2007; Schüssler & Vögler 2008; Steiner et al. 2008; Danilovic et al. 2010) particularly in the higher layers of the photosphere and low chromosphere. Here, we corroborate these findings with the simulation runs mentioned in Sect. 2.3.

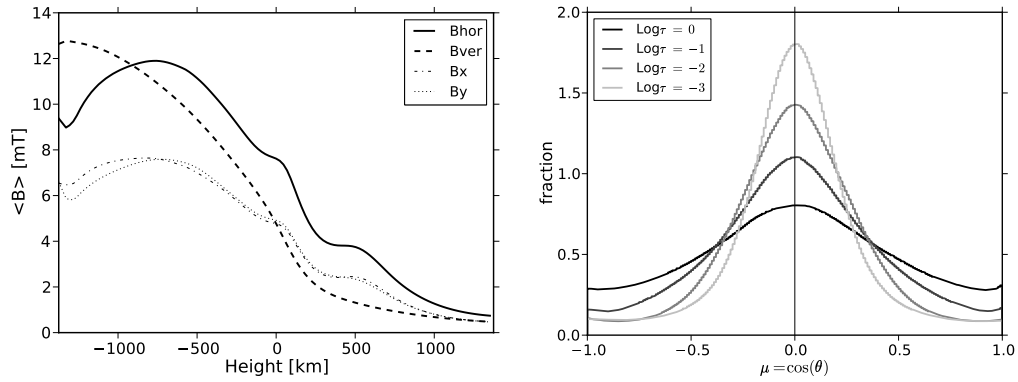


Figure 13. Left: Horizontally averaged strength of various magnetic field components as a function of geometrical height in the model atmosphere of simulation h50. Dashed: Vertical component, $\langle |B_v| \rangle$; Dot-dashed and dotted: Horizontal components $\langle |B_x| \rangle$ and $\langle |B_y| \rangle$; Solid: Horizontal component $B_h = \langle (B_x^2 + B_y^2)^{1/2} \rangle$. Right: Histogram for the cosine of the inclination of the magnetic field with respect to the vertical direction for different optical depth levels from $\log \tau = 0$ (broadest distribution), to $\log \tau = -3$ (narrowest distribution). An isotropic distribution would give a straight horizontal line.

Figure 13 shows in the left panel the horizontally averaged strength of various magnetic field component as a function of geometrical height in the model atmosphere of simulation h50. The dashed curve refers to the absolute value of the vertical component, B_v , the dotted and dash-dotted curves to the absolute value of the two horizontal components B_x and B_y which stand orthogonal to each other, and the solid curve to the horizontal component $B_h = (B_x^2 + B_y^2)^{1/2}$. The horizontal components surpass the vertical one throughout the photosphere from $z = 0$ to 500 km. They are particularly dominant at and closely above 500 km height. At $z = 500$ km $\langle B_h \rangle / \langle |B_v| \rangle(500 \text{ km}) = 2.9$ and $\langle B_{x,y} \rangle / \langle |B_{ver}| \rangle(500 \text{ km}) = 1.9$.

The panel on the right hand side of Fig. 13 shows the histogram for the cosine of the inclination of the magnetic field with respect to the vertical direction for different optical depth levels from $\log \tau = 0$ (broadest distribution), to $\log \tau = -3$ (narrowest distribution). An isotropic distribution would be represented by a straight horizontal line. Instead, the distributions are peaked at the 90° angle and become narrower with increasing height in the atmosphere, because of the increasing dominance of the horizontal component with height.

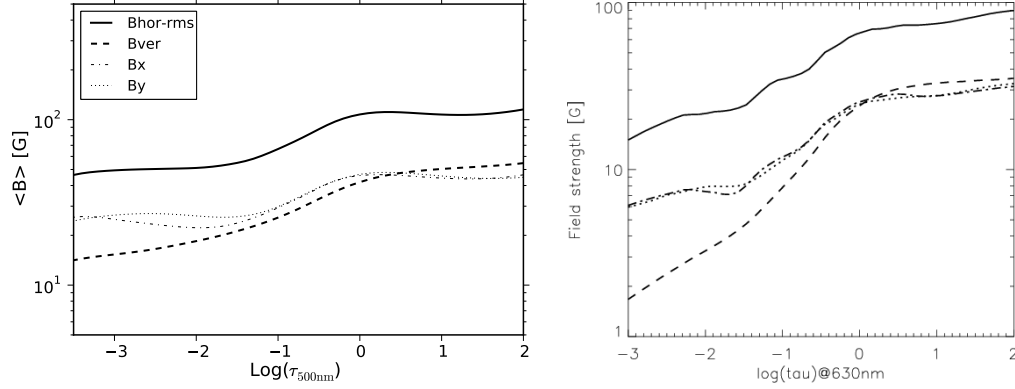


Figure 14. Horizontally averaged strength of various magnetic field components as a function of optical depth of the model atmosphere of simulation h50 (left) and the surface-dynamo simulation of Schüssler & Vögler (2008) (right, reproduced with permission © ESO). Dashed: Vertical component, $\langle |B_v| \rangle$; Dash-dotted and dotted: Horizontal components $\langle |B_x| \rangle$ and $\langle |B_y| \rangle$; Solid: Root-mean-square of the horizontal component $B_{\text{h,rms}} = (\langle B_x^2 + B_y^2 \rangle)^{1/2}$.

The situation is different for simulation v50. Even though, the horizontal components show distinct local maxima close to $z = 500$ km, the vertical component dominates for all heights. This is because of the initial condition of a homogeneous vertical magnetic field B_0 , which conserves the mean vertical field strength above the convection zone to B_0 for all times. Therefore, the ratio $\langle B_h \rangle / \langle |B_v| \rangle$ is basically predetermined by the initial condition in this case, which may be more representative of a network-field patch or a weak plage region.

Figure 14 shows a comparison between the simulations of Schüssler & Vögler (2008) (right panel) and the present result from simulation h50 (left panel). Again, the mean horizontal and vertical components are plotted, this time as a function of continuum optical depth and on a logarithmic scale. Despite the very different initial and boundary conditions and despite the different codes with which these simulations were carried out, the general trend is similar. In both simulations, the horizontal field component dominates throughout the photosphere. The absolute values of the field strength are different though: in case of the simulation h50, it depends on the strength of the horizontal field that is advected across the lower boundary (which is a boundary condition), in case of Schüssler & Vögler (2008) it depends on the efficiency of the surface dynamo, which in turn depends on the Reynolds numbers achieved by the simulation.

4. Summary and Conclusions

Vortical flows of mainly vertically directed vorticity have been observed to exist in the deep photosphere (Brandt et al. 1988; Wang et al. 1995; Bonet et al. 2008; Attie et al. 2009; Bonet et al. 2010; Balmaceda et al. 2010; Vargas Domínguez et al. 2011) and in the chromosphere (Wedemeyer-Böhm & Rouppe van der Voort 2009). Numerical simulations show particularly strong vortical flows immediately below the visible optical surface $\tau_c = 1$, beneath (the vertices of) inter-granular lanes. The centripetal force associated with these vortical flows is so strong that the gas pressure gradient opposing it

leads to a substantial reduction of the density within them, which may have observable consequences (Nordlund 1985; Kitiashvili et al. 2011; Moll et al. 2011). We find that there exists no one-to-one connection between the density deficient vortices in the surface layers of the convection zone and the observable vortical flows at $\tau_c = 1$, but one can assume the latter to extend and intensify with depth, simply because they are found within downdrafts and because of angular momentum conservation in combination with the gravitational stratification. This indicates that vortex stretching is probably an important source of vorticity in the surface layers although Shelyag et al. (2011) found the baroclinic vorticity generation to dominate in the convection zone and at the visible surface.

As was anticipated by Nordlund (1985) and Brandt et al. (1988), these vortical flows can be an important source of hydromagnetic disturbances. Magnetic field that is advected into vortices start to rotate. In the photosphere, where the thermal pressure generally dominates the magnetic energy density ($\beta \gg 1$), this can be considered a kinematic process, but vertically extending magnetic fields quickly start to dominate with height in the atmosphere. When $\beta \ll 1$, the rotating magnetic field now acts on the plasma via Lorentz force making it to rotate. Therefore, in the photosphere and in the chromosphere, the surface of $\beta = 1$ separates two regimes of vorticity generation (see also Fig. 3). In the regime, where $\beta \ll 1$ vortical flows of vertically directed vorticity is generated by vertically extending magnetic flux concentrations which root within vortical flows of the deep photosphere and the surface layers of the convection zone. Thus, while vorticity is generated by hydrodynamic processes (vortex stretching and baroclinic vortex generation) in the deep photosphere and the convection zone, it is mediated to the upper photosphere and chromosphere via magnetic fields. One can imagine that the formation of rotating magnetic flux concentrations may be the source of torsional Alfvén waves (Jess et al. 2009), which could potentially create a substantial Poynting flux in the outward direction, leading to coronal disturbances (but see (Routh et al. 2010) for the cutoff frequency of torsional tube waves) and having consequences for solar-wind acceleration and coronal heating in regions of open magnetic field configurations (Zirker 1993).

Granular lanes are composed of a leading bright rim and a trailing dark edge, which form at the boundary of a granule and move together into the granule itself. Virtually every granule harbors one or several granular lanes during its lifetime and they are well visible in high resolution broad band filtergrams of the solar surface. They are the visible manifestation of horizontally extending vortex tube found in numerical simulations (Steiner et al. 2010).

A more comprehensive view of vortices in the solar atmosphere reveals that there exists not only vertical and horizontal vortices (which are probably easiest to detect) but an unsteady network of highly tangled filaments of swirls, some of which protruding above the optical surface, for example in the form of arc shaped filaments (Moll et al. 2011).

Attempts to measure the angular distribution of the magnetic field in quiet regions and internetwork regions of the Sun (Lites et al. 2007, 2008; Orozco Suárez et al. 2007; Martínez González et al. 2008; Beck & Rezaei 2009; Asensio Ramos 2009; Danilovic et al. 2010; Stenflo 2010; Ishikawa & Tsuneta 2011; Borrero & Kobel 2012) have led to controversial results. Basic difficulties arise from the fact that in such regions, (i) the Zeeman splitting of spectral lines is much smaller than the line width because the field strength is mostly weak or spatially not resolved (small filling factor) so that the

field strength cannot be determined by simply measuring the Zeeman splitting. Instead, detailed radiation transfer and atmospheric modeling is required for correctly interpret polarimetric measurements. Even more problematic for the determination of the inclination angle is (ii) that the linear polarization depends in the weak field limit quadratically on the field strength while the circular polarization has a linear dependency. Since both polarization states are subject to a common noise level, the transversal field component is more severely affected by noise than the longitudinal component. Monte Carlo simulations with different noise levels added to synthesized Stokes profiles (Borrero & Kobel 2011) show, that a Stokes-inversion procedure may interpret pure noise as transversal fields with a strength of, e.g., 80 G for a noise level of $\sigma = 1.0 \times 10^{-3} I_c$. We propose a less biased determination of the mean horizontal to vertical field strength by applying a common noise criterion to the field strengths in the real physical domain instead of to signals in the Stokes space.

Establishing a bivariate scatter plot of the blue amplitudes of Stokes V of Fe I $\lambda\lambda$ 630.15 nm and 630.25 nm for each pixel of a quiet Sun region, reveals two populations of points (Stenflo 2010): (i) a population with a slope that is compatible with the weak field limit and (ii) a population that seems to be only compatible with kG fields. We have analyzed synthesized Stokes- V profiles from an MHD-simulation with the result that they too show the same two populations in corresponding scatter plots but cannot be explained in terms of intrinsically strong and weak fields. Rather, we find both populations stemming from intrinsically weak fields but from different locations. The population compatible with the weak field limit typically stems from clusters of pixels located within granules. The population that was formerly interpreted as being due to intrinsically strong field of small filling factors stems from pixels located at the boundaries between granules and the inter-granular space which harbor (weak) canopy fields with a field strength that abruptly increase with height in the atmosphere and show a downdraft in the deep photospheric layers (below the canopy field). So far, we have not analyzed the details of the radiation transfer that creates under these circumstances Stokes- V profiles that behave, regarding their amplitude ratio, like stemming from kG-fields but in reality originate from weak fields. The two lines Fe I $\lambda\lambda$ 630.15 nm and 630.25 nm do not form under the same conditions, in particular not at the same height in the atmosphere. Therefore, it can be either that the two lines sample different field strengths because of the canopy character of the field, which implies steep field gradients, or that they are differently affected by the downflows in the deep layers, creating different Stokes- V asymmetries, or that thermal effects play a role. From the present analysis we conclude that the two populations are *not* due to a dichotomy between “collapsed” and “uncollapsed” fields but due to a distinct difference in the formation of profiles and in the physical conditions at the location of the formation, i.e., the granule interiors and at the boundaries of granules, where canopy fields prevail. It is very likely, that this explanation also holds for the two populations of actually observed Stokes- V profiles.

Finally, we show, that a new simulation in which convective updrafts across the lower boundary advect horizontal fields of 50 G strength into the computational domain, yield a dominance of the horizontal vs. the vertical field throughout the photosphere, increasing with height. This is in agreement with and corroborates previous simulation results by Schüssler & Vögler (2008), Steiner et al. (2008), and Danilovic et al. (2010).

Acknowledgments. The authors acknowledge insightful discussions on small-scale filament formation within the ISSI International Team lead by Irina N. Kitiashvili at ISSI (International Space Science Institute) in Bern. We are grateful to Jan O. Stenflo for letting us use his IDL program for establishing line-ratio scatter plots and to Juan Manuel Borrero for various comments on the manuscript.

References

- Abbett, W. P. 2007, *ApJ*, 665, 1469
- Asensio Ramos, A. 2009, *ApJ*, 701, 1032. 0906.4230
- Attie, R., Innes, D. E., & Potts, H. E. 2009, *A&A*, 493, L13. 0811.3445
- Balmaceda, L., Vargas Domínguez, S., Palacios, J., Cabello, I., & Domingo, V. 2010, *A&A*, 513, L6. 1004.1185
- Barthol, P. (ed.) 2011, *The Sunrise Ballon-Borne Stratospheric Solar Observatory* (Springer)
- Beck, C., & Rezaei, R. 2009, *A&A*, 502, 969. 0903.3158
- Beeck, B., Collet, R., Steffen, M., Asplund, M., Cameron, R. H., Freytag, B., Hayek, W., Ludwig, H.-G., & Schüssler, M. 2012, *ArXiv e-prints*. 1201.1103
- Bonet, J. A., Márquez, I., Sánchez Almeida, J., Cabello, I., & Domingo, V. 2008, *ApJ*, 687, L131. 0809.3885
- Bonet, J. A., Márquez, I., Sánchez Almeida, J., Palacios, J., Martínez Pillet, V., Solanki, S. K., del Toro Iniesta, J. C., Domingo, V., Berkefeld, T., Schmidt, W., Gandorfer, A., Barthol, P., & Knölker, M. 2010, *ApJ*, 723, L139. 1009.1992
- Borrero, J. M., & Kobel, P. 2011, *A&A*, 527, A29. 1011.4380
- 2012, *A&A*. Submitted
- Brandt, P. N., Scharmer, G. B., Ferguson, S., Shine, R. A., & Tarbell, T. D. 1988, *Nat*, 335, 238
- Clyne, J., Mininni, P., Norton, A., & Rast, M. 2007, *New Journal of Physics*, 9, 301
- Danilovic, S., Schüssler, M., & Solanki, S. K. 2010, *A&A*, 513, A1. 1001.2183
- Freytag, B., Steffen, M., Ludwig, H.-G., Wedemeyer-Böhm, S., Schaffenberger, W., & Steiner, O. 2012, *Journal of Computational Physics*, 231, 919
- Goode, P. R., Yurchyshyn, V., Cao, W., Abramenko, V., Andic, A., Ahn, K., & Chae, J. 2010, *ApJ*, 714, L31
- Grossmann-Doerth, U., Schüssler, M., & Steiner, O. 1998, *A&A*, 337, 928
- Ishikawa, R., & Tsuneta, S. 2011, *ApJ*, 735, 74. 1103.5556
- Ishikawa, R., Tsuneta, S., & Jurčák, J. 2010, *ApJ*, 713, 1310. 1003.1376
- Jess, D. B., Mathioudakis, M., Erdélyi, R., Crockett, P. J., Keenan, F. P., & Christian, D. J. 2009, *Science*, 323, 1582. 0903.3546
- Keller, C. U., Solanki, S. K., Steiner, O., & Stenflo, J. O. 1990, *A&A*, 233, 583
- Khomenko, E., & Collados, M. 2007, *ApJ*, 659, 1726
- Kitiashvili, I. N., Kosovichev, A. G., Mansour, N. N., & Wray, A. A. 2011, *ApJ*, 727, L50. 1011.3775
- 2012, *ArXiv e-prints*. (ApJL, submitted), 1201.5442
- Lites, B., Socas-Navarro, H., Kubo, M., Berger, T., Frank, Z., Shine, R. A., Tarbell, T. D., Title, A. M., Ichimoto, K., Katsukawa, Y., Tsuneta, S., Suematsu, Y., & Shimizu, T. 2007, *PASJ*, 59, 571
- Lites, B. W., Kubo, M., Socas-Navarro, H., Berger, T., Frank, Z., Shine, R., Tarbell, T., Title, A., Ichimoto, K., Katsukawa, Y., Tsuneta, S., Suematsu, Y., Shimizu, T., & Nagata, S. 2008, *ApJ*, 672, 1237
- Lites, B. W., Leka, K. D., Skumanich, A., Martínez Pillet, V., & Shimizu, T. 1996, *ApJ*, 460, 1019
- Manso Sainz, R., Martínez González, M. J., & Asensio Ramos, A. 2011, *A&A*, 531, L9
- Martínez González, M. J., Asensio Ramos, A., López Ariste, A., & Manso Sainz, R. 2008, *A&A*, 479, 229. 0710.5219
- Martínez González, M. J., Manso Sainz, R., Asensio Ramos, A., & Bellot Rubio, L. R. 2010, *ApJ*, 714, L94. 1003.1255

- Moll, R., Cameron, R. H., & Schüssler, M. 2011, *A&A*, 533, A126. 1108.0800
 — 2012, ArXiv e-prints. (*A&A*, submitted), 1201.5981
- Muthsam, H. J., Kupka, F., Löw-Baselli, B., Obertscheider, C., Langer, M., & Lenz, P. 2010, *New Astron.*, 15, 460. 0905.0177
- Nordlund, Å.. 1985, *Solar Phys.*, 100, 209
- Orozco Suárez, D., Bellot Rubio, L. R., del Toro Iniesta, J. C., Tsuneta, S., Lites, B. W., Ichimoto, K., Katsukawa, Y., Nagata, S., Shimizu, T., Shine, R. A., Suematsu, Y., Tarbell, T. D., & Title, A. M. 2007, *ApJ*, 670, L61. 0710.1405
- Pötzi, W., & Brandt, P. N. 2007, *Central European Astrophysical Bulletin*, 31, 11
- Routh, S., Musielak, Z. E., & Hammer, R. 2010, *ApJ*, 709, 1297
- Ruiz Cobo, B. 2007, in *Modern solar facilities - advanced solar science*, edited by F. Kneer, K. G. Puschmann, & A. D. Wittmann (Universitätsverlag Göttingen), 287
- Sakurai, T. (ed.) 2008, *The Hinode Mission* (Springer)
- Schou, J., Scherrer, P. H., Bush, R. I., Wachter, R., Couvidat, S., Rabello-Soares, M. C., Bogart, R. S., Hoeksema, J. T., Liu, Y., Duvall, T. L., Akin, D. J., Allard, B. A., Miles, J. W., Rairden, R., Shine, R. A., Tarbell, T. D., Title, A. M., Wolfson, C. J., Elmore, D. F., Norton, A. A., & Tomczyk, S. 2011, *Solar Phys.*, 368
- Schüssler, M., & Vögler, A. 2008, *A&A*, 481, L5. 0801.1250
- Shelyag, S., Keys, P., Mathioudakis, M., & Keenan, F. P. 2011, *A&A*, 526, A5. 1010.5604
- Stein, R., & Nordlund, Å. 1998, *ApJ*, 499, 914
- Stein, R. F., & Nordlund, Å. 2006, *ApJ*, 642, 1246
- Steiner, O. 2000, in *Encyclopedia of Astronomy and Astrophysics*, edited by Murdin, P. (Taylor & Francis Group)
- 2010, in *Magnetic Coupling between the Interior and Atmosphere of the Sun*, edited by S. S. Hasan & R. J. Rutten (Springer), 166. 0904.2026
- Steiner, O., Franz, M., Bello González, N., Nutto, C., Rezaei, R., Martínez Pillet, V., Bonet Navarro, J. A., del Toro Iniesta, J. C., Domingo, V., Solanki, S. K., Knölker, M., Schmidt, W., Barthol, P., & Gandorfer, A. 2010, *ApJ*, 723, L180. 1009.4723
- 2011, in *4th Hinode Science Meeting: Unsolved Problems and Recent Insights*, edited by L. Bellot Rubio, F. Reale, & M. Carlsson, vol. 455 of *ASP Conference Series*, 35
- Steiner, O., Rezaei, R., Schaffenberger, W., & Wedemeyer-Böhm, S. 2008, *ApJ*, 680, L85. 0801.4915
- Stenflo, J. 1994, *Solar Magnetic Fields* (Kluwer Academic Publishers)
- Stenflo, J. O. 1973, *Solar Phys.*, 32, 41
- 2010, *A&A*, 517, A37
- 2011, *A&A*, 529, A42
- Vargas Domínguez, S., Palacios, J., Balmaceda, L., Cabello, I., & Domingo, V. 2011, *MNRAS*, 416, 148. 1105.3092
- Vögler, A. 2004, in *Reviews in Modern Astronomy*, edited by R. E. Schielicke, vol. 17 of *Reviews in Modern Astronomy*, 69
- Vögler, A. 2011, Ph.D. thesis, International Max Planck Research School, University of Braunschweig and Göttingen
- Vögler, A., Shelyag, S., Schüssler, M., Cattaneo, F., Emonet, T., & Linde, T. 2005, *A&A*, 429, 335
- Wang, Y., Noyes, R. W., Tarbell, T. D., & Title, A. M. 1995, *ApJ*, 447, 419
- Wedemeyer-Böhm, S., & Rouppe van der Voort, L. 2009, *A&A*, 507, L9. 0910.2226
- Wedemeyer, S., Freytag, B., Steffen, M., Ludwig, H.-G., & Holweger, H. 2004, *A&A*, 414, 1121. arXiv:astro-ph/0311273
- Wedemeyer-Böhm, S. 2008, *A&A*, 487, 399
- Yurchyshyn, V. B., Goode, P. R., Abramenko, V. I., & Steiner, O. 2011, *ApJ*, 736, L35. 1106.5535
- Zhang, J., & Liu, Y. 2011, *ApJ*, 741, L7. 1109.5003
- Zirker, J. B. 1993, *Solar Phys.*, 147, 47